HIGH-HARMONIC GENERATION IN THE RELATIVISTIC LAMBDA-CUBED REGIME

by

James Hamilton Easter

A dissertation submitted in partial fulfillment
of the requirements for the degree of
Doctor of Philosophy
(Electrical Engineering)
in The University of Michigan
2010

Doctoral Committee:

Professor Karl M. Krushelnick, Co-Chair
Emeritus Professor Gérard Mourou, Co-Chair
Assistant Professor Alexander G. R. Thomas
Adjunct Associate Professor John A. Nees

© James H Easter 2010

All Rights Reserved

To my parents

ACKNOWLEDGEMENTS

I'd like to thank all of the members of my committee. Gérard Mourou for his advice and encouragement, and for taking me in as a new student and assuring me that there would be opportunities for me at CUOS despite his departure. Karl Krushelnick for his advice and ideas. John Nees, especially for allowing me so much latitude in the projects I chose to pursue. And Alec Thomas for his constant interest in and help with my work.

I'd also like to thank Bixue Hou for all of the help he gave me in the lab, especially with the laser system. The harmonic experiment was a million times easier with Aghapi Mordovanakis' help and motivation. Also, the members of the Hercules team, especially Takeshi Matsuoka and Tolya Maksimchuck, provided a great deal of assistance (and equipment).

My whole graduate school experience has been much more enjoyable with the friends I've had inside and outside of work: the guys I've shared an office and killed too much time with; all of the other graduate students I know, of whom there are too may too list here, especially those who joined the EECS optics program with me in 2004; and members of the taekwondo club.

Finally, I'd like to thank my parents and siblings for their encouragement and support, even after I left them all on the East Coast.

TABLE OF CONTENTS

CHAPTER

LIST OF FIGURES

Figure

LIST OF TABLES

Table

LIST OF APPENDICES

Appendix

CHAPTER I

Introduction

The work presented in this thesis covers a wide range of projects that, if presented independently, would have seemingly little in common. However, when presented in order, each project is shown to build on the previous ones, all leading up to the ultimate goal: high-repetition-rate, high-harmonic generation from solid targets in the relativistic regime achieved by tight focusing of low-energy ultrashort pulses.

1.1 The λ^3 regime

All of the work presented in this thesis was performed in the λ^3 lab at the Center for Ultrafast Optical Science (CUOS), University of Michigan. The purpose of the λ^3 system is to make relativistic laser-plasma experiments accessible without the need for a massive laser facility. By reducing the focal spot size to approximately one square wavelength (λ^2) and the pulse duration to approximately one cycle ($1/\nu$) all of the pulse energy can be confined to a volume of approximately one cubic wavelength: $\lambda^2(c/\nu) = \lambda^3$. This allows very high intensities ($> 10^{18}$ W/cm^2) to be achieved with very small energies ($\sim$1 mJ). Consider the intensity of 1 mJ of 800 nm light with a single-cycle pulse duration, τ, and single wavelength focus size, w_0:

$$I \approx \frac{E}{\tau w_0^2} = \frac{1\ \mathrm{mJ}}{(800\ \mathrm{nm}/c)(800\ \mathrm{nm})^2} \approx 6 \times 10^{19}\ \mathrm{W/cm^2} \tag{1.1}$$

This is well above the relativistic threshold for 800 nm light of 2×10^{18} W/cm^2. By operating at such low pulse energies the size and repetition rate of the system are much more favorable. The λ^3 system fits on two standard optical tables and has a repetition rate of 500 Hz. In fact, similar systems with multikilohertz repetition rates are now commercially available.

1.2 Dissertation outline

In the first chapter, the design and implementation of a high-ASE contrast regenerative amplifier are described. Sufficient contrast is necessary in high-intensity laser experiments to avoid the formation of an expanding plasma prior to the arrival of the main pulse.

In Chapter III, an ultrashort pulse measurement technique is proposed and tested. This technique is a modification of an existing pulse measurement method, multiphoton intrapulse interference phase scan (MIIPS). The new method simplifies spectral phase measurements by employing pre-existing components in the amplifier system. The single beam nature of MIIPS allows spectral phase measurements to be made under more realistic, even in situ, experimental conditions.

The minimum pulse duration of systems such as λ^3 is limited to approximately 20 fs by gain narrowing in the amplifier. Filamentation compression is an increasingly popular technique for shortening amplified pulses to the sub-10 fs range. The experiment discussed in Chapter IV extends the filamentation technique to higher energies, potentially raising the achievable λ^3 intensity closer to 10^{20} W/cm^2.

One of the most challenging aspects of working in the λ^3 regime is obtaining a high quality single wavelength focus. The λ^3 system utilizes a high-numerical aperture paraboloidal mirror and adaptive optics to produce its tight focus. Chapter V presents a new method for optimizing the adaptive optics to produce the highest possible focused intensity.

Finally, in Chapter VI all of the previous work leads to the production of high-harmonics from solid target experiments.

CHAPTER II

High ASE Contrast Regenerative Amplifier

2.1 Introduction

In high-intensity laser experiments, radiation arriving prior to the main pulse is capable of ionizing material and forming a preexisting plasma. The properties of this "pre-plasma" can have a significant effect on the interaction of the main pulse. One of the most important properties of the pre-plasma is its density scale-length, usually defined as

$$L = n \left(\frac{dn}{dz} \right)^{-1} \tag{2.1}$$

where n is the density. In general, the earlier the plasma is formed and the higher the intensity of the light that formed it, the longer the scale-length will be.

In high-power laser systems, there are three primary sources of energy arriving before the main pulse: amplified spontaneous emission (ASE), the "pedestal," and pre-pulses. In any amplifier, the spontaneous emission undergoes gain along with the pulse being amplified. ASE exists for as long as gain is available ($\sim$3 μs in Ti:Sapphire). Switching optics can suppress very early ASE, but it will always exist for a few, or even a few hundred, nanoseconds before the main pulse and is often strong enough to ionize materials. The pedestal is an energy ramp in the picosecond time range that occurs in chirped pulse amplification (CPA) systems when phase errors during stretching and compression temporally scatter energy that should have been in the main pulse [1]. Finally, pre-pulses are additional compressed pulses caused by multiple reflections or scattering of the main beam from optics in the system.

The strengths of the ASE, pedestal, and pre-pulses are usually characterized by the contrast ratio of the main pulse intensity to their own. Because the scale-length can be intentionally increased to control the parameters of the interaction (e.g. by the introduction of a controlled pre-pulse), it is usually desirable to have as high a contrast ratio as possible. A number of techniques exist for improving the contrast ratio, including saturable absorption [2], cross-polarized wave generation (XPW) [3], frequency doubling [4], and plasma mirrors [5]. All of these techniques require extra amplification stages or lossy post-amplification processes. For the case of ASE, an alternative or complementary approach to improving the contrast is to specifically design the amplifier to produce very little ASE to begin with.

2.2 Design

The λ^3 system is a millijoule level, titanium sapphire, chirped pulse amplification (CPA) system. A schematic diagram is shown in Fig. 2.1.

Prior to the work described in this thesis the λ^3 amplification stage consisted of a 6-pass, high gain amplifier followed by a 3-pass power amplifier. In designing the new, low ASE amplifier, both stages were replaced by a single regenerative amplifier (Fig. 2.2). Injection and dumping is performed by a single Pockels cell (PC1) and a pair of thin film polarizers. The cryogenically cooled Ti:Sapphire crystal is pumped from both sides by a pair of intracavity frequency-doubled Nd:YLF lasers (Spectra-Physics Evolution-30 and Evolution-X) with a total of 30 mJ of energy at 527 nm. Concave cavity end mirrors with a 3 m radius of curvature at 2.5 m from the crystal

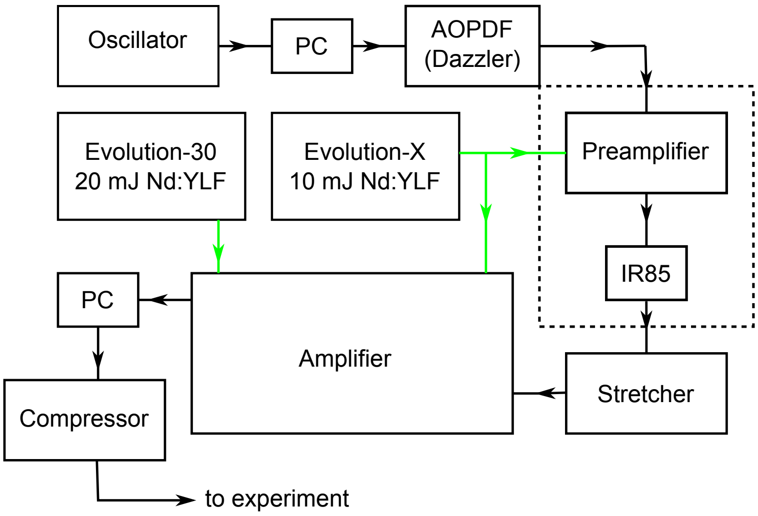

Figure 2.1: λ^3 laser system diagram. PC: Pockels cell; IR85: saturable absorber.

produce a free space Gaussian mode size (w_0) of 500 μm.

The key design concept behind the λ^3 regenerative amplifier is to use a mode with a very low divergence angle. All other parameters being equal, the divergence angle of the amplifier mode determines how much spontaneous emission will be collected and amplified. The instantaneous power of the spontaneous emission immediately after pumping can be expressed as

$$P_{SE} = \frac{E_{pump}}{\lambda_{seed}/\lambda_{pump}} \frac{1}{\tau} \tag{2.2}$$

where E_{pump} is the total pump energy, λ_{seed} is the lasing wavelength, λ_{pump} is the pump wavelength, and τ is the lifetime of the gain medium. The ratio $(\lambda_{seed}/\lambda_{pump})^{-1}$ is the quantum defect of the gain medium and expresses what fraction of the pump energy is available for gain at the lasing wavelength.

The spontaneous emission power expressed in Eq. (2.2) is emitted isotropically into a solid angle of 4π sr. However, the cavity collects only that radiation emitted into a solid angle comparable to that of the lowest order mode:

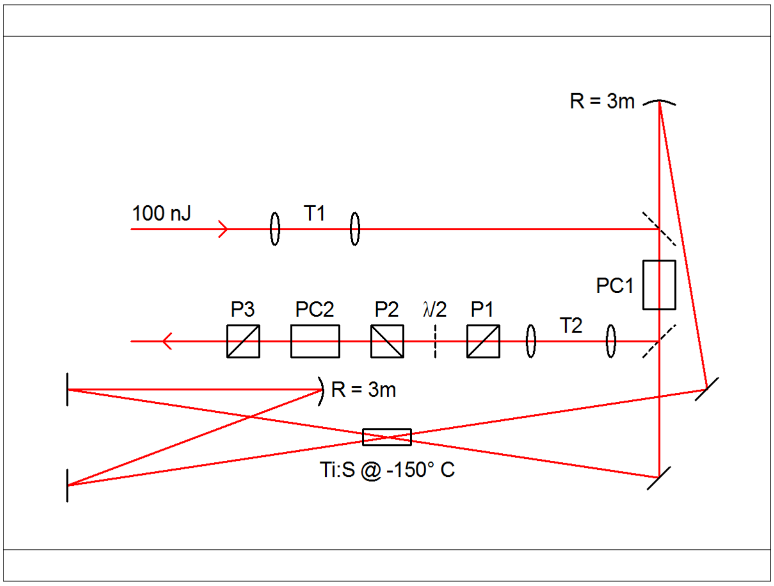

Figure 2.2: Diagram of the λ^3 regenerative amplifier. T1: input telescope; PC1: Pockels cell for injection and dumping; R: concave mirrors; T2: output telescope; P1, P2, P3: polarizers; PC2: pulse-cleaning Pockels cell.

$$\Omega_0 = \pi \left(\frac{\lambda_{seed}}{\pi w_0} \right)^2 \tag{2.3}$$

where w_0 is the free space waist size of the fundamental cavity mode. The collected solid angle is reduced by an additional factor of $n^3_{crystal}$ due to refraction at the faces of the Brewster-cut crystal (the factor is only $n^2_{crystal}$ for a crystal at normal incidence). Combining Eqs. (2.2) and (2.3), dividing by the isotropic 4π sr, and including the extra solid angle factor gives the total collected spontaneous emission power:

$$P_{SE,collected} = \frac{E_{pump}}{\lambda_{seed}/\lambda_{pump}} \frac{1}{\tau} \pi \left(\frac{\lambda_{seed}}{\pi w_0} \right)^2 \frac{1}{4\pi} \frac{1}{n^3_{crystal}} \tag{2.4}$$

The w_0^{-2} dependence of the ASE is the motivating factor for working with a large mode size and has been briefly discussed in regard to similiar amplifier designs [6]. The variables of Eq. (2.4) and their values for the λ^3 system are shown in Table 2.1.

Inserting these values into Eq. (2.4) yields a collected spontaneous emission power of 70 W.

E_{pump}	30 mJ	τ	3 μs
λ_{seed}	800 nm	w_0	500 μm
λ_{pump}	527 nm	n_{crystal}	1.8

Table 2.1: Parameters of the λ^3 regenerative amplifier.

The λ^3 system can be operated with and without the preamplifier and saturable absorber. Without them the seed energy for the regenerative amplifier is ∼1 nJ. With them the seed energy is increased to ∼100 nJ. In either case the number of roundtrips in the cavity is adjusted to deplete the gain, giving the same output energy.

The contrast can be estimated by comparing the collected spontaneous emission power (70 W) to the power of the seed. Because both signals experience approximately the same gain, their ratio stays constant throughout amplification. However, the random spectral phase of the spontaneous emission prevents it from being compressed, so the ratio of interest is actually that of the spontaneous emission to that of the compressed seed. Assuming a compressed pulse duration of 30 fs, the powers of the seed with and without the preamplifier are 3.3 MW and 33 kW, respectively. The expected ASE contrast ratios are therefore 3.3 MW/70 μW $= 5 \times 10^{10}$ and 33 kW/70 μW $= 5 \times 10^{8}$.

2.3 Testing

In operation the λ^3 regenerative amplifier requires 11 round trips to deplete the gain. Fig. 2.3 shows a typical trace of the energy buildup in the cavity. The buildup and the necessary round trips varied according to the alignment of the cavity and the output of the pump lasers. In general the system is capable of delivering approximately 3 W (6 mJ per pulse) to the compressor gratings.

A third order autocorrelator (Fig. 2.4) was used to measure the ASE, the pedestal,

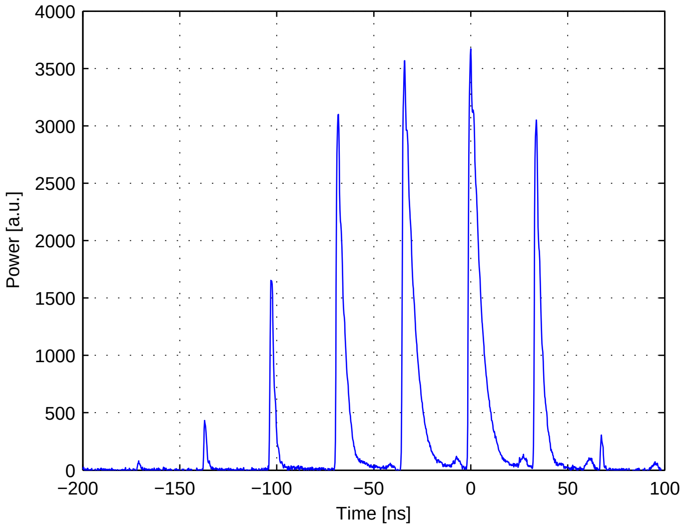

Figure 2.3: Regenerative amplifier buildup trace. The pulse shown here is dumped one or two round trips late to demonstrate the saturation and subsequent loss.

and the prepulses (Fig. 2.5). The autocorrelation was performed with the preamplifier and saturable absorber in operation.

At negative delays, postpulses in the second harmonic arm of the autocorrelator can overlap with pulses in the fundamental arm, leading to the appearance of prepulses. All of the prepulses in Fig. 5 can be matched to such postpulses, most of which are generated by multiple reflections in the BBO crystals and BG39 filter.

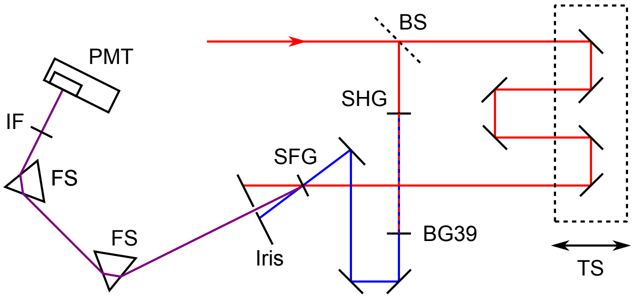

Figure 2.4: Third order autocorrelator. BS: beamsplitter; TS: translation stage; SHG: 10 μm BBO crystal for second harmonic generation; SFG: 50 μm BBO crystal for sum frequency generation; BG39: 3 mm BG39 glass filter; FS: fused silica Brewster prisms; IF: (267 ± 5) nm interference filter; PMT: photomultiplier tube.

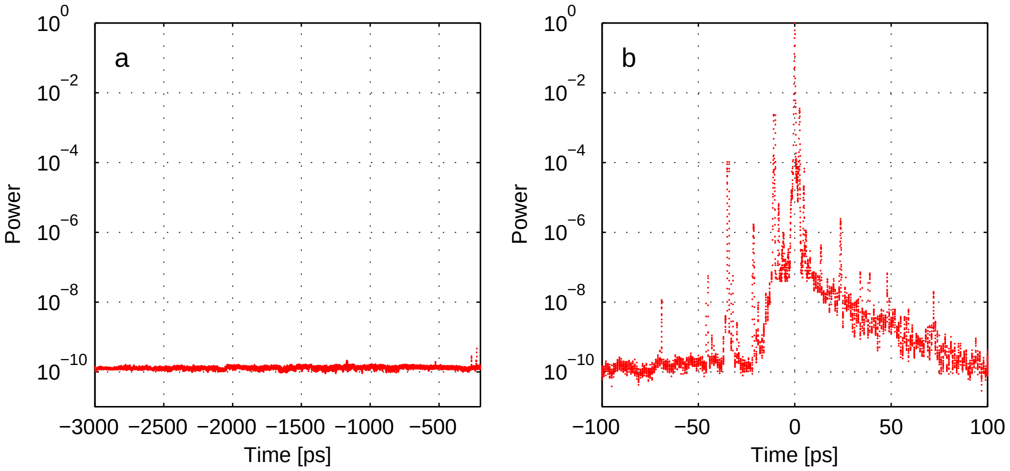

Figure 2.5: Third order autocorrelation showing nanosecond scale contrast (a) and picosecond scale contrast (b).

Real prepulses can be generated inside CPA systems by the nonlinear transfer of postpulse energy [7]. Postpulses that fall within the stretched pulse duration (∼30 ps in the λ^3 system) will undergo nonlinear mixing with the main pulse via $\chi^{(3)}$ processes, generating weaker, mirror images of themselves before the main pulse. Unfortunately, the postpulses that cause this effect will also appear as artificial prepulses in the third order autocorrelation. Because the artificial prepulses and the real prepulses occur at the same delay, it is impossible to distinguish them. None of the resolvable prepulses in Fig. 2.5 that fall within the stretched pulse duration can be attributed to this effect. If they exist—and they must—they are either weaker than the pedestal or obscured by the artificial prepulses.

From Fig. 2.5, the measured ASE contrast is $(1.2 \times 10^{-10})^{-1} = 8.3 \times 10^{9}$. This is a factor of 6 worse than the predicted contrast of 5×10^{10}. This is due to a few factors: (i) The gain of the spontaneous emission is higher than that of the main pulse due to saturation. If the majority of this difference occurs in the last pass of gain, then it should be approximately equal to a single pass of gain, about 2. (ii) The system amplifies only about half of the bandwidth of the seed due to gain narrowing. (iii)

Decay traces of the seeded, unpumped amplifier show that approximately 20–30% of the seed is lost due to its spatial quality when coupling to the cavity. Combined, these three factors reduce the expected contrast by a factor of 5, matching the measured contrast very well.

Experimentally it was found that the contrast of the system without the preamplifier and saturable absorber was sufficient for generating short scale-lengths on glass targets. A third order autocorrelation was not performed without the preamplifier. Only the strength of the ASE is expected to change along with the strength of the seed. The source of the other major contrast feature, the pedestal that begins rising at ∼20 ps, was discussed earlier. The pedestal is generated by uncorrectable spectral phase noise in the stretcher and compressor [1], which is unaffected by the absence of the preamplifier.

A simple photodiode measurement of the ASE was performed without the preamplifier and saturable absorber. The amplifier was operated under normal conditions but with the seed blocked. The full beam before the compressor was collected by a lens and measured using a standard silicon photodiode with a response time of ∼1 ns. Terminated into 50 Ω, the peak of the signal was 300 mV. Three neutral density filters totaling (5.6 ± 0.1) OD were used to attenuate the beam. Using the manufacturer specified responsivity of 0.4 A/W at 800 nm, the peak power of the ASE could be calculated as

$$P = \frac{1}{T}\frac{1}{\mathcal{R}}\frac{V}{R} = 10^{-5.6}\frac{1}{0.4}\frac{300\text{ mV}}{50\ \Omega} = 6\text{ kW} \tag{2.5}$$

where T is the transmission of the filters, $\mathcal{R}$ is the responsivity, V is the voltage and R is the termination resistance.

The pulse into the compressor has an energy of 6 mJ and a compressible pulse duration of 30 fs, giving a power of 2×10^{11} W. The contrast ratio is therefore 2×10^{11} W/6 kW $= 3.3 \times 10^{7}$. The predicted gain without the preamplifier is about a factor of 100 lower than that measured by the third order autocorrelator (Fig. 2.5): $8.3 \times 10^{9}/100 = 8.3 \times 10^{8}$. The photodiode measurement was performed without a seed, eliminating the effect of gain depletion. Assuming most of the depletion occurs during a single pass, the measured ASE is approximately a factor of 2 higher than it would be with a seed. Scaling the measured ASE by this factor gives a contrast ratio of 6.6×10^{7}, which matches well with the predicted contrast.

The ASE contrast of the λ^3 system prior to this modification was 1×10^{8} [1]. The improved contrast from the regenerative amplifier (8.3×10^{9}) is approximately 80 times higher. Also, the contrast without the preamplifier and saturable absorber (6.6×10^{7}) is less than a factor of 2 lower.

The goal of the λ^3 system is to achieve on-target relativistic intensities above 2×10^{18} W/cm^2. If the contrast ratio is taken to be 6×10^{7}, then the on-target ASE intensity will be 3.3×10^{10} W/cm^2. The final Pockels cell of the system allows approximately 5 ns of ASE through before the main pulse. The damage threshold of fused silica for 5 ns pulses is (140 ± 60) J/cm^2 [8] or an intensity of $(2.8 \pm 1.2) \times 10^{10}$ W/cm^2, which is close to the measured ASE intensity depending on the accuracy of the measurements and the quality of the surface.

2.4 Conclusion

In conclusion, a high ASE contrast regenerative amplifier was designed, constructed and tested. By increasing the mode size of the cavity the amount of spontaneous emission collected was reduced. The predicted ASE contrast matched well with a third order autocorrelation and a simple photodiode measurement. The improvement in ASE contrast compared to the previous 2-stage multipass amplifier was approximately a factor of 80. The system is operated primarily without the preamplifier and saturable absorber. Under these conditions, the ASE intensity is similar to the measured damage threshold of fused silica. However, high-harmonic experiments have shown that the contrast is sufficient for short scale-length interactions on SiO_2 targets (see Chapter VI). For more demanding target materials (e.g. metals), an increase in ASE contrast of approximately 100 can be achieved by employing the preamplifier and saturable absorber.

CHAPTER III

Grating-based Multiphoton Intrapulse Interference Phase Scan

3.1 Introduction

The measurement of ultrashort optical pulses is a subject of ongoing research. The fundamental difficulty in measuring ultrashort pulses is the lack of a shorter probe. When a shorter probe is available, measurements are straightforward. When a shorter probe is not available, one must resort to indirect methods in which pulses are used to measure themselves. A host of techniques have been developed to do just this. Some, such as second and third-order autocorrelations, are fairly simple but rely on significant assumptions about the shape of the pulse. Spectral interferometry for direct electric field reconstruction (SPIDER) [9] is a powerful technique for measuring the spectral phase of ultrashort pulses, but it has low resolution and requires a high signal-to-noise ratio. A third technique, frequency resolved optical gating (FROG) [10], is capable of measuring both the amplitude and phase of ultrashort pulses, but in most cases it requires a fairly complex setup.

All of these techniques-and others-have their advantages and disadvantages. The choice of measurement depends largely on the situation. The pulse energy, wavelength, beam quality, and other factors all play a role in determining the appropriate technique. A fourth technique, multiphoton intrapulse interference phase scan (MIIPS) [11], is a relative newcomer to the field of pulse measurement, but is well-suited to the needs of a λ^3 type system.

3.2 MIIPS theory

The theory behind multiphoton intrapulse interference phase scan is very simple. Start with an expression for the spectral power of a second harmonic signal:

$$S(2\omega) = \left| \int_{-\infty}^{\infty} E(\omega + \Omega) E(\omega - \Omega) d\Omega \right|^2 \tag{3.1}$$

which is simply the autoconvolution of the fundamental electric field, $E(\omega)$. Then, separate the field into its magnitude, $|E(\omega)|$, and phase, $e^{\varphi(\omega)}$:

$$S(2\omega) = \left| \int_{-\infty}^{\infty} |E(\omega + \Omega) E(\omega - \Omega)| e^{i\varphi(\omega+\Omega)+i\varphi(\omega-\Omega)} d\Omega \right|^2 \tag{3.2}$$

The two phase terms in Eq. (3.2) can be expanded in a Taylor series to second order about Ω:

$$\varphi(\omega \pm \Omega) \approx \varphi(\omega) \pm \varphi'(\omega)\Omega + \frac{1}{2}\varphi''(\omega)\Omega^2 \tag{3.3}$$

Summing the two expansions yields

$$\varphi(\omega + \Omega) + \varphi(\omega - \Omega) \approx 2\varphi(\omega) + \varphi''(\omega)\Omega^2 \tag{3.4}$$

Using the approximation of Eq. (3.4) in Eq. (3.2) yields

$$S(2\omega) = \left| \int_{-\infty}^{\infty} |E(\omega+\Omega)E(\omega-\Omega)| e^{i2\varphi(\omega)+i\varphi''(\omega)\Omega^2} d\Omega \right|^2 \tag{3.5}$$

$$= \left| \int_{-\infty}^{\infty} |E(\omega+\Omega)E(\omega-\Omega)| e^{i\varphi''(\omega)\Omega^2} d\Omega \right|^2 \tag{3.6}$$

where the constant phase term $i2\varphi(\omega)$ has been pulled out of the integral and eliminated by the absolute value. Looking at Eq. (3.6), it is obvious that the second harmonic signal will be maximized when $\varphi''(\omega) = 0$ and the exponential is unity. Physically this means that the signal at any particular second harmonic frequency 2ω is maximized when the group delay dispersion (GDD) at the corresponding fundamental frequency ω is zero. The approximation of Eq. (3.4) is actually two approximations in disguise: (i) the phase is slowly varying over a sufficiently small frequency range, and (ii) widely spaced fundamental frequency components do not strongly contribute to the signal at their sum frequency. To see how the condition on the GDD can be used we consider the phase, $\varphi(\omega)$, to be the sum of an intrinsic phase (i.e. the phase being measured), $\phi(\omega)$, and a known phase that is intentionally applied as part of the MIIPS process, $\theta(\omega)$:

$$\varphi(\omega) = \phi(\omega) + \theta(\omega) \tag{3.7}$$

The condition $\varphi''(\omega) = 0$ implies that

$$\phi''(\omega) = -\theta''(\omega) \tag{3.8}$$

That is, in order to maximize the second harmonic signal at 2ω, the applied GDD, $\theta''(\omega)$, must exactly cancel the intrinsic GDD, $\phi''(\omega)$, at ω. The phase of the pulse can then be obtained by simple integration:

$$\phi(\omega) = \iint\limits_{\omega_0}^{\omega} \phi''(\omega) d\omega = - \iint\limits_{\omega_0}^{\omega} \theta''(\omega) d\omega \tag{3.9}$$

The procedure for using MIIPS is therefore to apply a known spectral phase to the pulse being measured, frequency double that pulse, determine the GDD that maximizes the second harmonic signal at each frequency, then integrate.

3.3 Implementation

The applied phase, $\theta(\omega)$, can come from any source as long as it is known and spans the range of GDD required to cancel the intrinsic GDD, $\phi''(\omega)$, at every frequency being measured. Traditionally the phase has been applied using a spatial light modulator (SLM) inside an f-to-f grating arrangement [11] (Fig. 3.1a).

This has the advantage of allowing the spectral phase to be both measured and corrected to high order. However, there are three significant downsides to this approach. The first is that SLMs cannot generally be used following amplification. The efficiency of SLMs is usually several tens of percent. Not only does this sacrifice a significant amount of amplified energy, it also limits the power that an SLM can handle. Not being able to employ the device after amplification leads to the second downside of using SLMs for MIIPS. In any amplifier operating above ∼1 mJ, a non-negligible amount of self phase modulation (SPM) can occur during amplification. Any spectral phase applied prior to amplification will not be linearly mapped to the spectral phase on the pulse at the output of the amplifier, leading to errors in the phase retrieval. The third downside to using SLMs is their expense and complexity.

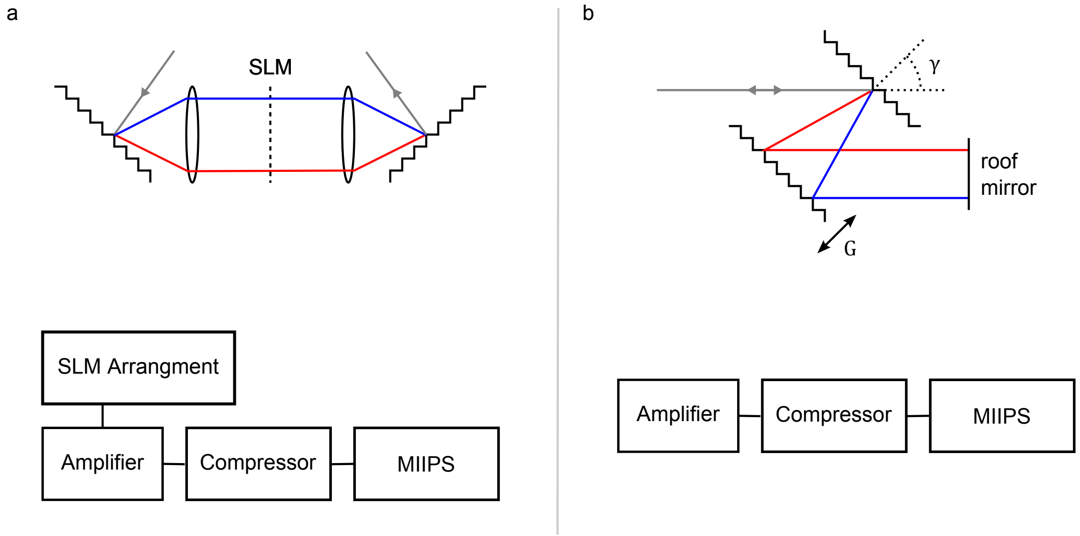

Figure 3.1: Dispersive elements for MIIPS pulse measurement. (a) A programmable SLM prior to amplification. (b) An adjustable grating compressor following amplification.

It was noted above that any method of applying spectral phase is acceptable as long as the GDD spans the necessary range. Any number of devices could potentially satisfy this criterion including SLMs, prisms, chirped mirrors, acousto-optic dispersive devices, and grating pairs. Grating pairs (Fig. 3.1b) have some unique advantages over other devices when measuring short pulses from typical chirped pulse amplification (CPA) systems. First, many, if not most, CPA systems already contain a pair of gratings at the end to perform compression. Second, the grating compressor is situated at the end of the system after any SPM has occurred, so the applied spectral phase is not distorted by any nonlinearity. Finally, since the gratings are already part of the system, no additional loss needs to be introduced. The GDD of a double-passed grating pair is [12]

$$\theta'' = -G\frac{N^2\lambda^3}{\pi c^2 \cos^3\beta} \tag{3.10}$$

where G is the perpendicular separation between gratings, N is groove density, λ is

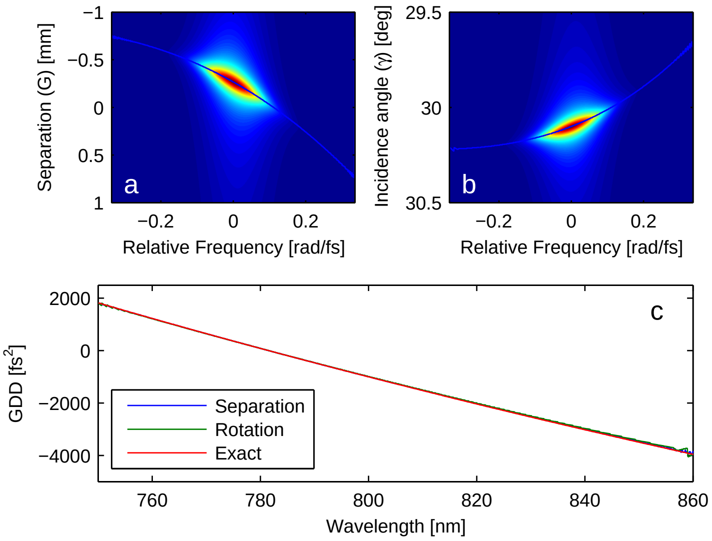

Figure 3.2: Simulated MIIPS traces demonstrating the use of grating separation (a) versus grating rotation (b). (c) The retrieved GDD for both methods plotted against the exact GDD.

the wavelength, c is the speed of light, and β is the diffracted angle according to the grating equation:

$$\sin\gamma - \sin\beta = m\lambda N \tag{3.11}$$

where γ is the incidence angle and m is the order of diffraction (almost always 1 for a compressor pair). From Eq. (3.10) one can see that there are two possible means of scanning the GDD of a grating pair: changing the separation and changing the angle. In principle, changing the angle of the gratings affects their reflectivity, which would cause errors in the phase retrieval, but in practice, the angle change is usually too small to effectively alter the reflectivity. Fig. 3.2 shows simulated MIIPS traces of a transform limited pulse obtained by scanning (a) the separation and (b) the rotation.

3.4 Advantages and disadvantages

Most of the advantages of MIIPS are derived from its simplicity. One of the simplicities of MIIPS is that it depends not on the absolute value of any spectral component, but on the occurrence of a maximum. This is especially advantageous for pulses with large bandwidths, over which the response of optics, detectors, and the SHG process itself can vary significantly. The efficiency of second harmonic generation [13], for example, can be expressed as

$$R(\omega) = \left[\omega\chi^{(1)}(\omega)\chi^{(1)}(\omega/2)\mathrm{sinc}\left(\frac{\Delta k(\omega/2,\omega/2)L}{2}\right)\right]^2 \tag{3.12}$$

where ω is the frequency at the second harmonic, $\chi^{(1)}$ is the linear susceptibility of the crystal, L is the length of the crystal, and Δk is the phase mismatch between the fundamental and second harmonic:

$$\Delta k(\omega_1,\omega_2) = k(\omega_1) + k(\omega_2) - k(\omega_1+\omega_2) \tag{3.13}$$

Eq. 3.12 has been plotted in Fig. 3.3 for several different type-I crystals. This efficiency must be accounted for in broadband FROG measurements to yield accurate results. For sufficiently large bandwidths, the wings of a spectrum might fall where the SHG efficiency is very low, leading to large uncertainties if the R factor is not precisely known. However, when performing a MIIPS measurement, this frequency dependent “filter” is irrelevant. The GDD that produces the maximum at each frequency is independent of the shape of $R(\omega)$. This independence also applies to the spectral response of the spectrometer, any filters used and optics, eliminating many sources of systematic error.

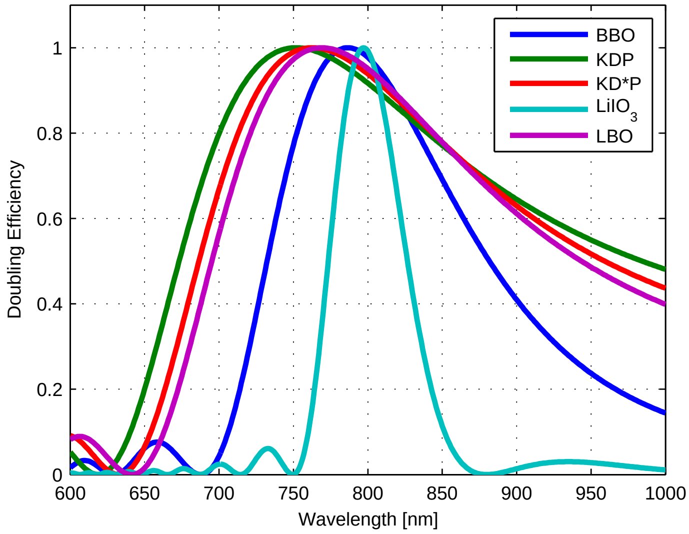

Figure 3.3: Type-I second harmonic efficiency for several different nonlinear crystals. All crystals are 10 μm thick. The crystal angle was chosen independently for each crystal to maximize efficiency near 800 nm.

Another advantage of MIIPS is the fact that it uses only a single beam. This allows pulse measurements to be performed in situ, further eliminating systematic errors. Multiple beam techniques must take into account the tabulated or measured dispersion of beamsplitters and other optics. By replacing a target or sample with a doubling crystal, a single beam MIIPS measurement can be performed that introduces no additional dispersion and contains all of the inherent dispersion of the delivery optics.

While MIIPS is a remarkably powerful technique, especially given its simplicity, there are some disadvantages, including: (i) introducing positive and negative GDD is difficult without the inherent control of dispersion devices found in amplifiers, (ii) it is not single shot and (iii) it can be inaccurate for complicated phases.

Inherent dispersive devices make MIIPS straightforward in CPA systems. However, the measurement of isolated pulses is difficult. In most cases, small amounts of both positive and negative GDD must be applied. A grating pair can only be used when the large total GDD is used to compress an initially chirped pulse and differential GDD is applied near the compression point. Likewise, the SLM concept relies on knowledge of the GDD difference as the pixels are modulated, not on the total GDD of the system. Prism arrangements can provide adjustable GDD of both signs, but are not as easy to adjust as gratings or SLMs. A rotating etalon can also provide adjustable GDD of both signs, but the complex, oscillatory nature of etalon dispersion can introduce errors in the phase retrieval, as discussed below.

In theory, MIIPS could be implemented in a single shot fashion by imposing varying dispersion across a uniform beam. The dispersion of an etalon in a converging or diverging beam offers one possibility. However, no single shot MIIPS implementation has been demonstrated. On the other hand, single shot autocorrelations and FROG measurements are of similar complexity to their standard designs.

Finally, the approximation made in Eq. (3.4) can introduce GDD retrieval errors for complicated phases. The higher the order of the inherent phase, the greater the retrieval error will be [14]. Fig. 3.4 shows simulated, grating-based MIIPS retrievals for four different orders of phase, 2nd (GDD) through 5th. In the figures on the right, the retrieved GDD (red) for 2nd and 3rd order phase is indistinguishable from the exact GDD (green). For 4th and 5th order phase, the retrieved GDD begins to deviate from the exact values. Higher order phases will be retrieved with increasing error.

3.5 Experiments

The λ^3 system uses a standard grating pair compressor following amplification, consisting of two gold-coated, 1200 grooves/mm gratings and a roof mirror (Fig. 3.5). The second grating is mounted on a manually actuated linear translation stage, while the pair is situated on a manually actuated rotation stage. The incidence angle was measured very accurately by rotating the gratings until second order Littrow diffraction of a collinear HeNe was achieved.

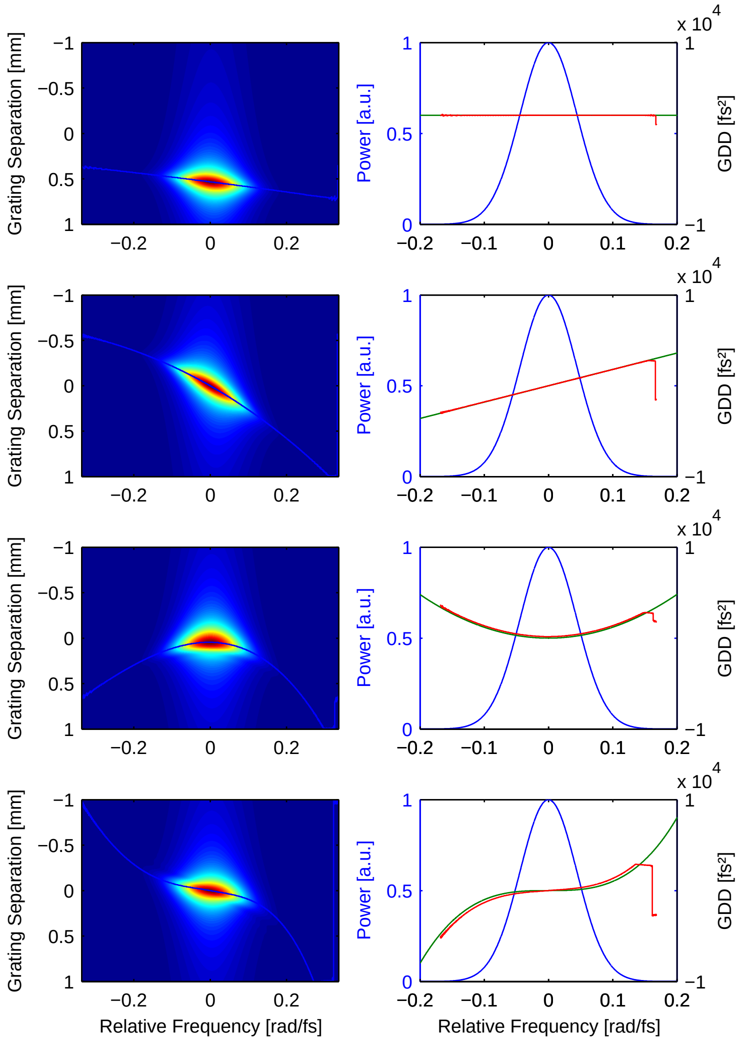

Figure 3.4: Simulated grating MIIPS GDD retrieval for various orders of phase (top to bottom): 500 fs^2, 500 fs^3, 417 fs^4 and 417 fs^5. Figures on the left are the second harmonic spectra as a function of frequency and relative grating separation. The blue curve tracks the optimum grating separation for each frequency. Figures on the right show the fundamental pulse spectrum (blue), the exact GDD (green) and the retrieved GDD (red).

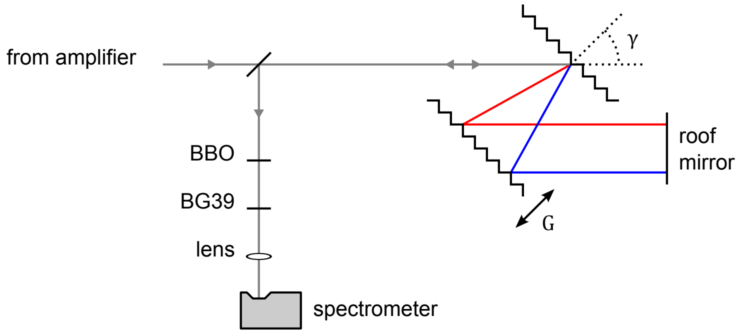

Figure 3.5: Grating based MIIPS arrangement.

The bandwidth of the amplified pulses is approximately 30 nm (FWHM). A 10 μm thick BBO crystal cut for type-I frequency doubling is used. A 3 mm thick BG39 filter is used to block the fundamental light. The second harmonic beam is then focused by a 5 cm focal length achromatic doublet. The doublet is not designed for the second harmonic spectrum, but because MIIPS does not depend on the relative intensity of the colors, any wavelength dependent coupling into the spectrometer due to the focusing optic is irrelevant. The focused spectrum is recorded with a miniature USB spectrometer (OceanOptics USB4000). The spectrometer has a resolution of approximately 1 nm.

In order to verify the accuracy of the technique, two different MIIPS measurements were made (Fig. 3.6): one in which the grating separation was scanned (Fig. 3.6a), the other in which the grating rotation was scanned (Fig. 3.6b). The λ^3 system contains a programmable acoustic dispersion device (Fastlite Dazzler), but the pulse was allowed to have large, uncorrected phase errors for the purpose of this measurement.

The calculated group delays are shown in Fig. 3.7a and their difference is shown in Fig. 3.7b. Over most of the spectrum the error was less than 5 fs out of a full range of almost 200 fs. Large errors occur only in the wings of the spectrum where the power is too low to accurately find a maximum. The agreement is expected to be better if a larger set of data is acquired. Unfortunately, at the time of this experiment, both the separation and rotation of the compressor were manually actuated, making

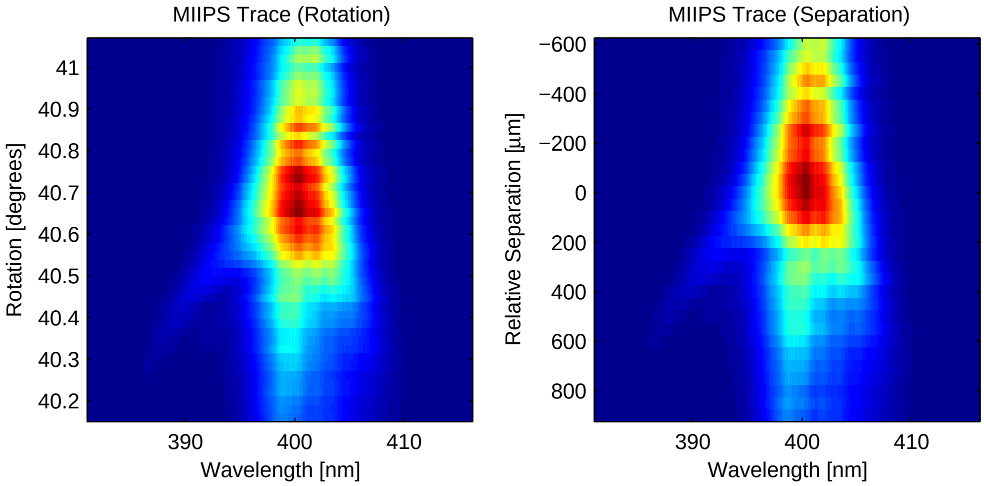

Figure 3.6: MIIPS traces acquired using (a) grating separation and (b) grating rotation.

it prohibitive to acquire data at more than about 100 points.

Fig. 3.8a a shows an independent measurement of the pulse spectrum and the spectral phase, obtained by integrating the group delay. The resulting temporal pulse shape based on both techniques (separation and rotation) is shown in Fig. 3.8b. The agreement is very good in terms of peak power, pulse width, and satellite structure.

3.6 Noise effects

Noise is a factor that affects any experimental measurement. To estimate the effect of noise on a MIIPS trace we consider the measurement of a transform limited pulse. If the applied phase is purely second order then the pulse will simply be stretched and compressed and the doubling efficiency at every color will be proportional to the pulse duration. If the pulse is stretched by a factor of two, then the second harmonic signal will be reduced by a factor of two. If the pulse is stretched by only ten percent, then the second harmonic signal will be reduced by a factor of approximately ten percent. This leads to an approximate rule regarding the error caused by signal noise. If the fundamental pulse has energy fluctuations of ∼2% (typical for a low

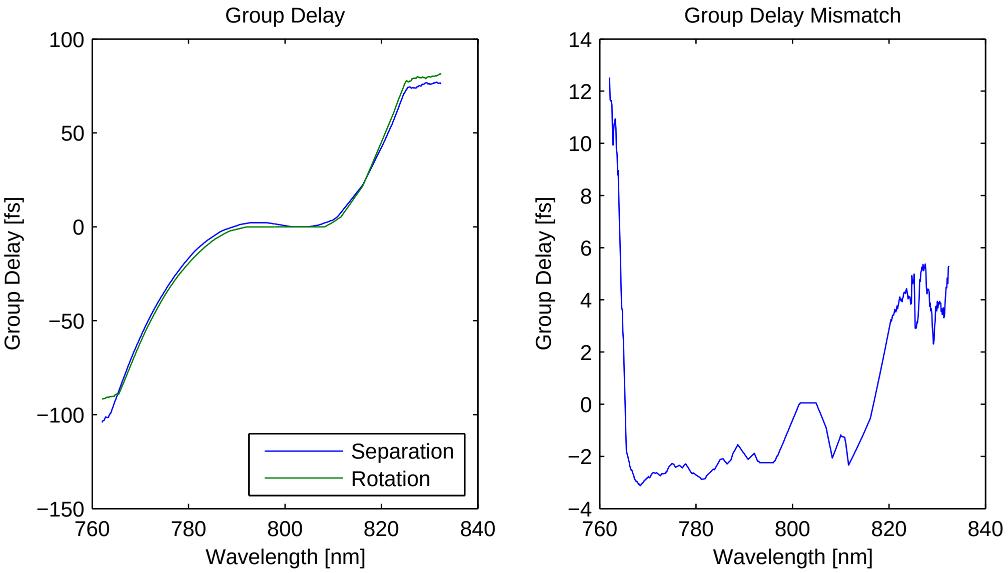

Figure 3.7: (a) Calculated group delays from the traces in Fig. 11. (b) Difference in group delay between the separation and rotation measurements.

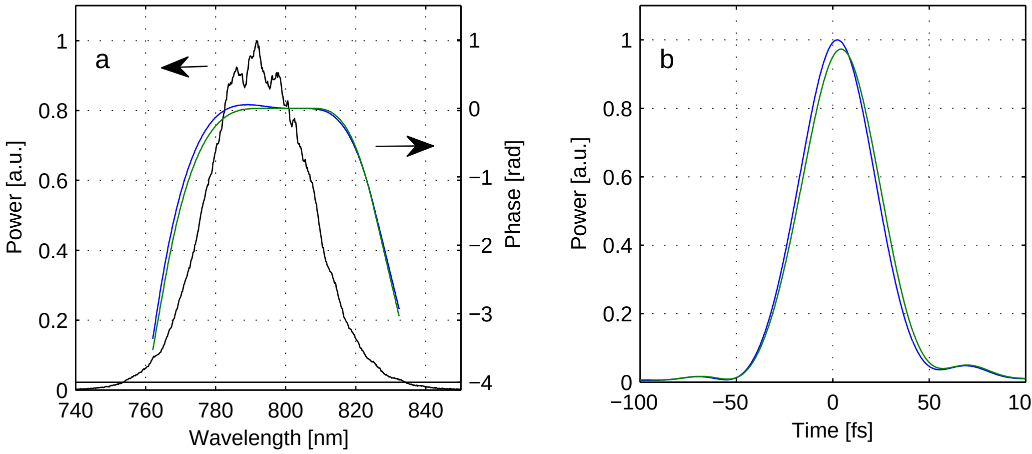

Figure 3.8: (a) Fundamental pulse spectrum and spectral phase. (b) Temporal pulse shapes based on the retrieved spectral phase from both techniques. In both figures, blue corresponds to the measurement by separation and green to the measurement by rotation.

energy CPA system) then the second harmonic signal will have fluctuations of ∼4%, so the expected error in the measured pulse duration would be around 4%. In fact, the error should be smaller since the integrations average the fluctuations over multiple values.

3.7 Conclusions and future work

In conclusion, the MIIPS pulse measurement technique has been demonstrated using the dispersion of standard grating pair compressor. Grating compressors are common to most amplified ultrashort pulse systems, making MIIPS accessible with no additional components. The agreement between two separate measurements using the separation and rotation of the gratings confirmed the accuracy of the technique. Advantages and disadvantages of MIIPS, retrieval errors, and noise sensitivity were discussed.

Immediate future work includes automating the translation and/or rotation stages to allow faster acquisition and denser sampling. This will not only make the measurement easier, but also improve the accuracy by allowing for smaller steps. In addition, an automated system could be coupled to an energy diagnostic allowing shot-to-shot fluctuations to be corrected for, further improving the measurement accuracy.

Additional work could include implementing other methods of applying phase. One of the downsides to grating pairs is the large total dispersion they introduce. This dispersion is not an issue when the gratings are already part of the system, but if one wishes to measure a pulse independent of the amplifier system then gratings are not appropriate. A device that applies a small amount of phase (both positive and negative GDD) is necessary. One possibility is an etalon. The sinusoidal positive and negative phase of an etalon can be scanned by rotation, and a Girres-Tournaeau etalon has unity power reflection.

CHAPTER IV

Filamentation Compression

4.1 Introduction

The ability to amplify ultrashort pulses is limited largely by gain narrowing [15] in high gain amplifiers. Typical millijoule level chirped pulse amplification (CPA) systems with gains on the order of 10^6 cannot produce pulses much shorter than about 30 fs. Spectral shaping prior to amplification [16] or inside the amplifier cavity [17] can be used to reduce pulse durations to approximately 20 fs. Optical parametric CPA (OPCPA) systems have been demonstrated for shorter pulse durations [18], but these systems are significantly more complex than standard CPA systems.

A significant effort has been made during the last two decades to develop post-amplification pulse compression techniques. Perhaps the simplest technique involves passing high intensity pulses through a solid material leading to self-phase modulation induced spectral broadening [19]. Subsequent phase correction allows the new spectral components to be aligned, shortening the pulse. However, this technique suffers from strong spatial inhomogeneities.

Confining the pulse helps reduce the spatial inhomogeneity problem. This is the concept behind spectral broadening in gas-filled hollow core fibers. Hollow core fibers with inner diameters of $\sim$200 μm provide weak confinement via grazing incidence reflection. Fibers of approximately 1 m length filled with a (usually) noble gas can lead to significant spectral broadening. Subsequent phase compensation (e.g. using chirped mirrors) can produce pulses shorter than 10 fs [20]. The downside to hollow core fibers is their limited energy capacity ($\sim$1 mJ), coupling sensitivity, and need for additional dispersion compensation.

A similar approach has been demonstrated in which self-focusing provides the confinement in a gas free of any external structure [21]. A pulse with power above the critical power of the surrounding gas will be focused by Kerr-lensing. As the pulse intensity climbs it begins to ionize the gas, forming a plasma. The shape of the plasma leads to a phenomena known as plasma defocusing. At some point the Kerr-lensing and plasma defocusing will balance each other causing the beam to propagate without diffracting, in the form of a "filament." Eventually energy loss and redistribution destroy the balance and cause the beam to defocus. During this process, SPM and other nonlinear effects produce additional bandwidth just as in a gas-filled fiber. The advantages of the filamentation technique are the lack of coupling sensitivity, the greater simplicity of the apparatus, and the fact that under the correct conditions the pulse will compensate its own phase, requiring no additional dispersion [22].

It should be noted that the processes involved in filamentation are not completely agreed upon. It has recently been demonstrated that simulations utilizing negative higher order nonlinear terms ($\chi^{(5)}$, $\chi^{(6)}$, ...) are able to better describe filamentation even without considering plasma effects [23].

One of the downsides to filamentation compression is instability. If the power is sufficiently far above the critical power of the gas then the focusing beam can break into multiple filaments, where the power of each filament is above the critical power. It has been shown that this instability can be reduced by introducing astigmatism in the focusing beam [24] (e.g. by rotating the focusing lens). An alternative method for reducing beam instability is to eliminate SPM prior to the point where focusing and defocusing are balanced.

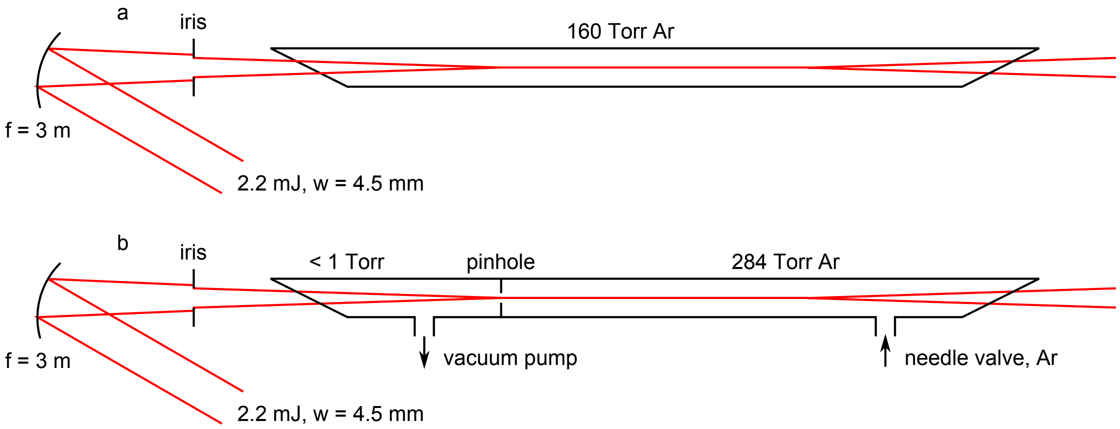

Figure 4.1: Comparative filamentation geometries. (a) Standard static pressure filamentation arrangement and (b) pinhole-initiated filamentation arrangement.

4.2 Experiment

Fig. 4.1 shows a diagram of the filamentation experiment performed on the λ^3 laser system. 2.2 mJ pulses with a 33 nm FWHM bandwidth centered at 800 nm were focused by a 6 m ROC dielectric mirror into a 1 in diameter tube. An adjustable iris was placed before the focusing lens allowing minor adjustment of the $f/\#$. The collimated beam size at the mirror was 4.5 mm (Gaussian beam radius). The mirror was placed as close as possible to the output of the compressor to avoid SPM in the air. The windows on the filamentation tube were 500 μm thick fused silica. Thicker windows would have introduced undesirable SPM. Thinner windows would have had poorer wavefront quality and may not have withheld the pressure difference during evacuation of the tube. Two different filamentation configurations were employed: (i) the tube was filled with a static gas (Fig. 4.1a) and (ii) a 700 μm diameter pinhole separated two sections of the tube, before and after focus, maintaining a constant pressure of gas on the far side while the focusing side was kept evacuated (Fig. 4.1b). The separation of the gratings in the compressor of the laser system was adjusted in all cases to produce the broadest output spectrum.

4.3 Pressure gradient

The goal of the pinhole-initiated filament is to enter the filamentation regime immediately, avoiding spatial distortion caused by gradual self-focusing. Therefore, it is desirable to have a steep pressure gradient at the pinhole, where the pulse instantly transitions from linear focusing in vacuum to the balanced filamentation regime. To determine if this was the case, the steepness of the pressure gradient at the pinhole was investigated by numerically solving the Navier-Stokes equations (Eqs. (4.1) and (4.2)) using a finite element analysis package.

$$\rho\mathbf{u}\cdot\nabla\mathbf{u} = \nabla\cdot[-\rho\mathbf{I} + \eta(\nabla\mathbf{u} + (\nabla\mathbf{u})^{\mathrm{T}}] \tag{4.1}$$

$$\nabla\cdot\mathbf{u} = 0 \tag{4.2}$$

In Eqs. (4.1) and (4.2) ρ is the density, $\mathbf{u}$ is the velocity, $\mathbf{I}$ is the identity matrix, and η is the viscosity. Fig. 4.2 shows the solution of the Navier-Stokes equations for a cylindrically symmetrical geometry with a 1 in diameter tube and a 1 mm long, 1 mm diameter pinhole. The pressures at the tube boundaries (500 mm in either direction) were fixed to 0 Torr and 300 Torr. The pressure, integrated over the 500 μm radius of the pinhole is shown in Fig. 4.3. The pressure drops from 90% to 10% in approximately 800 μm. Given that the Rayleigh range of the focusing system is ~11 cm, an 800 μm rise distance for the pressure can be considered nearly instantaneous.

4.4 Spectrum

In all cases, as the pressure in the tube is increased the spectral broadening also increases. However, the maximum pressure is limited by spatial and spectral stability.

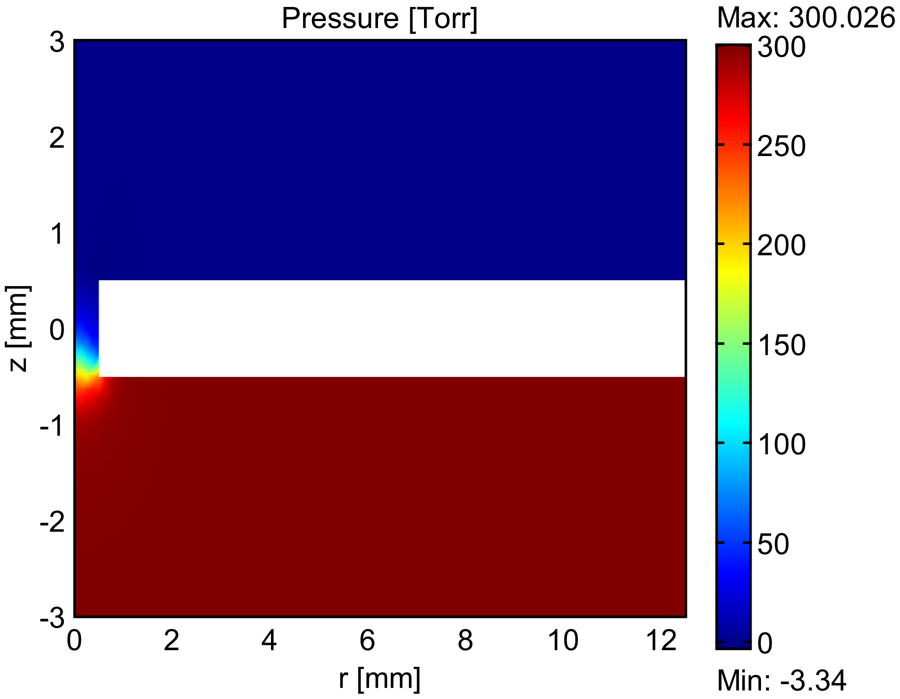

Figure 4.2: Finite element analysis of the pressure gradient across the pinhole.

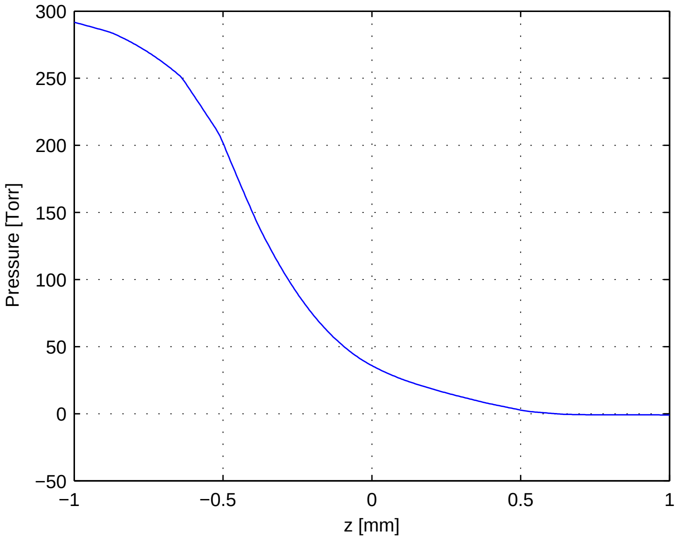

Figure 4.3: Pressure across filament pinhole. Values were integrated over the entire 500μm radius of the pinhole.

When the pressure is taken too high the beam begins to form multiple, unstable filaments and the spectrum, especially in the wings, also becomes unstable.

Spectra were acquired with the aid of an integrating sphere. The integrating sphere allowed the spectrum of the entire beam to be sampled, even when the beam was highly unstable and contained multiple filaments. The beam was collected by the integrating sphere immediately after exiting the output window of the filamentation tube. A miniature spectrometer (Ocean Optics USB4000) with a spectral range of 500 nm to 1100 nm was placed at the output port of the integrating sphere to record the spectrum. The integration time of the spectrometer was 30 ms (15 pulses).

In the case of filamentation with static gas pressure, the maximum pressure of argon for a stable filament was 160 Torr. The output spectrum for this case is shown by the blue curve in Fig. 4.4b. For the case of pinhole-initiated filamentation, the maximum pressure of argon for a stable filament was 284 Torr. This led to much greater spectral broadening (Fig. 4.4a). Two other configurations were tested to determine the effect of the pinhole (Table 4.1). To provide a more direct comparison of the two scenarios, the pressure without a gradient was increased to 284 Torr (Table 4.1 row 4). The spectrum is shown by the red curve in Fig. 4.4b. The spectrum has stronger short wavelength components, but does not extend as far into the longer wavelengths, nor is it as smooth on either side as the pinhole-initiated filament spectrum. In addition, the spectrum at 284 Torr without a gradient is very unstable.

When the system was operated with a pinhole and no gas (Table 4.1 row 2) the energy throughput was only 1.8 mJ. This suggests that a significant amount of energy was distributed well outside of the main focal spot and blocked by the pinhole. To make sure that this energy loss was not responsible for the stability at 284 Torr, the pinhole-free system was operated at 284 Torr with a reduced input energy of 1.7 mJ. However, the filament was still unstable, demonstrating that the pinhole does not stabilize the system by reducing the energy.

Pinhole	Pressure [Torr]	Output Energy [mJ]	Stable	Spectrum	Profile
yes	284	1.7	yes	Fig. 4.4a	Fig. 4.6a
yes	0	1.8	yes	-	-
no	160	2.1	yes	Fig. 4.4b (blue)	-
no	284	2.1	no	Fig. 4.4b (red)	Fig. 4.6b

Table 4.1: Filamentation configurations.

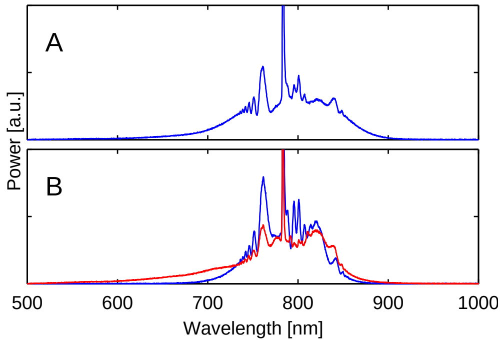

Figure 4.4: Output filamentation spectra. (a) Pinhole-initiated spectrum at 284 Torr. (b) Spectra with no pinhole at 160 Torr (blue) and 284 Torr (red).

The spectra are replotted in Fig. 4.5a along with their transform limited temporal profiles (Fig. 4.5b). Despite having 20% less energy, the pinhole-initiated spectrum supports a transform-limited pulse with 30% higher peak power than the pinhole-free spectrum.

The spatial profiles of the three configurations are compared in Fig. 4.6. The beam following filamentation was attenuated by near normal reflection from a glass wedge and scattered by a white card. The card was then imaged by a CCD coupled with a standard zoom lens. While the pinhole-free filament at 160 Torr produced a stable beam, its profile was not very symmetric (Fig. 4.6a). Increasing the pinhole-free pressure to 284 Torr produced a much lower divergence beam (Fig. 4.6b), but it was highly unstable. The pinhole-initiated filament at 284 Torr produced the most symmetric beam profile (Fig. 4.6a). The improvement over the stable, pinhole-free filament at 160 Torr is partly due to the spatial filtering performed by the pinhole.

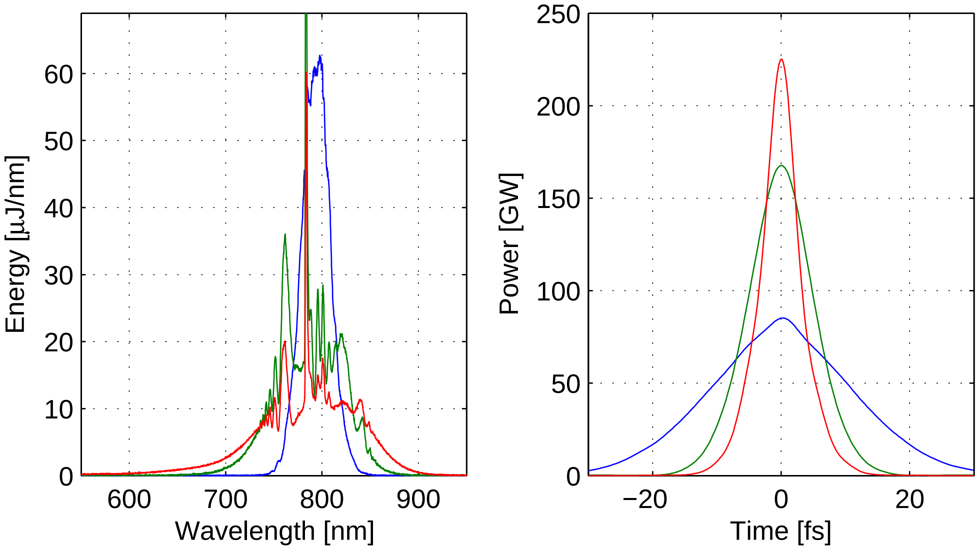

Figure 4.5: Spectra (a) and transform-limited pulse shapes (b) for the original spectrum (blue), pinhole-free at 160 Torr (green) and pinhole-initiated at 284 Torr (red).

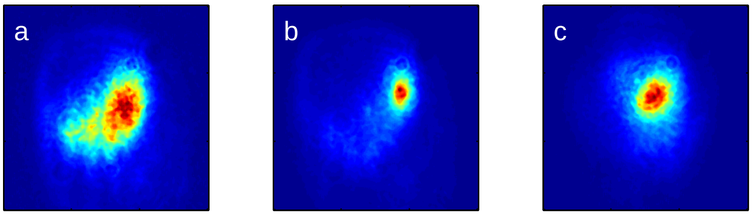

Figure 4.6: Spatial profiles of the beam for (a) pinhole-free at 160 Torr (stable), (b) pinhole-free at 284 Torr (unstable) and (c) pinhole-initiated at 284 Torr (stable).

4.5 Conclusion and future work

The use of a pressure differential was demonstrated to improve the spectrum and beam quality during filamentation compression. By eliminating self-focusing in the converging beam, spatial and spectral stability were maintained at a higher gas pressure. The higher gas pressure led to greater spectral broadening and therefore a potentially shorter pulse duration. A throughput of 1.7 mJ with a spectrum supporting 6.4 fs (FWHM) transform-limited pulses was achieved.

Measurement and correction of the spectral phase must still be performed before the pulses can be used. In addition, high order phase distortions were present in the original spectrum when this work was performed. A programmable dispersive device (Fastlite Dazzler) has been added to the λ^3 system subsequent to these measurements. Correction and control of the original spectral phase is expected to improve the spectral power and phase of the filamentation output.

In addition, the λ^3 system is being upgraded with the addition of a second amplification stage, which is expected to increase the compressed pulse energy to > 10 mJ. Filamentation compression has never been demonstrated at such a high pulse energy, but the pinhole-initiated concept may make it possible. If spectral broadening similar to that shown here can be achieved using 10 mJ pulses the final pulse power may exceed 1 TW.

CHAPTER V

Focus Optimization

5.1 Introduction

The fundamental component for achieving relativistic intensities in the λ^3 system is the high-NA off-axis paraboloid. Unfortunately, the production of high quality paraboloids is difficult. Off-axis paraboloids can have significant wavefront aberrations compared to conventional spherical optics. Well-corrected, transmissive aspheric optics and microscope objectives are available, but these components are highly dispersive and incapable of handling millijoule, ultrashort pulses. In addition, when trying to achieve diffraction limited focusing, wavefront aberrations in the system due to spherical lenses, thermal lensing, and self-phase modulation can become significant.

The problem of correcting wavefront distortions is well known in the field of astronomy. The Earth's atmosphere causes a significant amount of wavefront distortion, limiting the resolution of terrestrial telescopes. To correct for the aberrations of the atmosphere, high resolution telescopes utilize adaptive optics that reshape the incoming wavefront [25]. Using reference beams to measure the distortions caused by the atmosphere, adaptive optics can compensate for these distortions and produce much higher quality images.

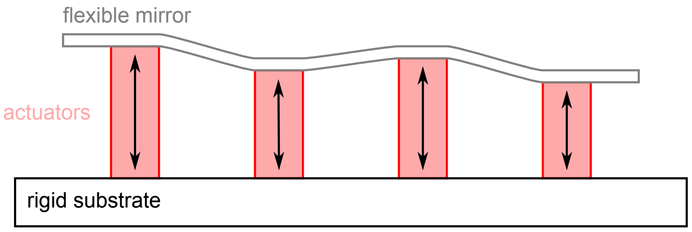

Figure 5.1: Diagram of a deformable mirror employing a solid, flexible surface and piezoelectric style actuators.

5.1.1 Deformable mirrors

One of the most common types of adaptive optics is the deformable mirror. By connecting a very thin mirror to an array of programmable actuators, the mirror surface can be deliberately and predictably deformed (Fig. 5.1). Various types of actuators can be used depending on the application requirements (e.g. range, speed, linearity, and hysteresis). Piezoelectrics are a popular choice for deformable mirror actuation due to their relatively low cost and fast response time.

5.1.2 Deformable mirrors in laser experiments

The laser community has adopted deformable mirrors for multiple uses, including the optimization of high-NA, high-intensity focusing. One of the challenges of implementing a DM is determining the appropriate mirror shape. Multiple approaches have been developed including direct measurement of the wavefront [26], optimization of second harmonic generation (SHG) in a nonlinear crystal [27] and in situ optimization of SHG at a surface [28].

Each technique has advantages and disadvantages. Direct wavefront measurement is fast but requires an expensive wavefront measurement device (e.g. Shack-Hartmann or shearing interferometer). Optimization of SHG in a crystal uses relatively simple components but requires a slow, iterative algorithm. Optimization of in situ surface SHG is free of aberrations introduced by additional optics, but requires very sensitive detection and a slow algorithm.

One disadvantage common to all three of these techniques is the need to significantly attenuate the pulse energy to avoid damage to optics. Attenuation not only introduces wavefront distortions from the attenuation optics (usually reflective or absorptive neutral density filters), but also modifies the wavefront distortions due to thermal and nonlinear effects. A second, shared disadvantage is that the plane of optimization is fixed by the alignment of the optics. The Rayleigh range of a high-NA focus is on the order of a few microns. Proper alignment of diagnostics for an optimization routine must match this sensitivity. Also, prior to wavefront correction, the proper position of the focus may not be clear.

An alternative to the methods above is to optimize SHG in a rarefied gas. The second order polarization of a plasma can be written as [29]

$$\mathbf{P}(2\omega) = \chi \left[(\mathbf{E} \cdot \nabla)\mathbf{E} + \frac{i\omega}{c}\mathbf{E} \times \mathbf{B} \right] + \frac{e\mathbf{E}(\nabla \cdot \mathbf{E})}{8\pi m \omega^2} \tag{5.1}$$

where $\chi = n_e e^3/4m^2\omega^4$. For a neutral plasma $\nabla \cdot (\epsilon_p \mathbf{E}) = 0$ with $\epsilon_p = 1 - \omega_p^2/\omega^2$ and Eq. (5.1) can be rewritten as

$$\mathbf{P}(2\omega) = \chi \left[\frac{1}{2}\nabla \mathbf{E}^2 + 2\frac{1}{\epsilon_p}\mathbf{E}(\mathbf{E} \cdot \nabla \ln n_e) \right] \tag{5.2}$$

The gradient term has zero curl and therefore cannot radiate. The second term describes a nonlinear polarization proportional to the electron density gradient, $\nabla \ln n_e$, and the square of the fundamental field. An electron density gradient is produced by the ponderomotive force:

$$f = -\frac{e^2}{4m\omega^2}\nabla_\perp E^2 \tag{5.3}$$

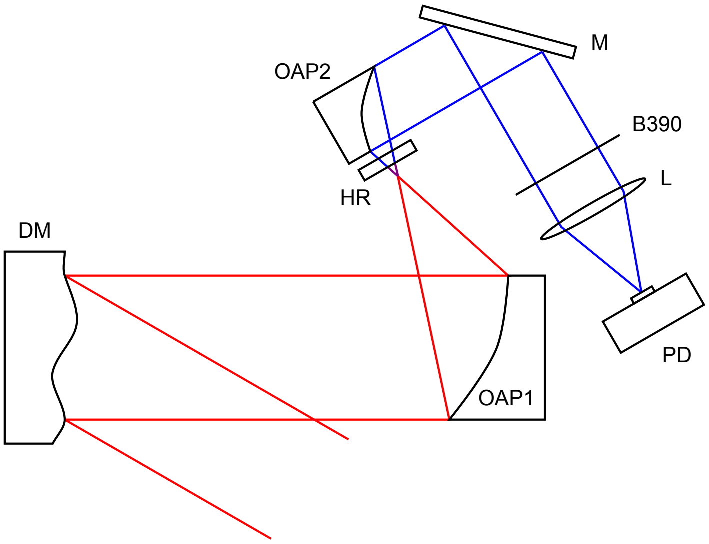

Figure 5.2: Focusing and collection setup for optimization of the deformable mirror via SHG in helium. DM: deformable mirror; OAP1: 2 in diameter, $f/1.4$, gold-coated off-axis paraboloid; HR: 800 nm high-reflector; OAP2: 1 in diameter, $f/1$, aluminum-coated off-axis paraboloid; M: flat, silver mirror; B390: 3 mm thick Hoya B390 filter; L: lens; PD: silicon photodiode.

Second harmonic generation in air by this mechanism has been demonstrated using 270 fs pulses at an intensity of 10^{15} W/cm^2 [30].

5.2 Experiment

The λ^3 system contains a 2 in diameter, silver coated deformable mirror (Xinetics) between the compressor and the paraboloid (Fig. 5.2). The mirror is controlled by an array of 49 piezolectric actuators. After being expanded to 9 mm (FWHM) by a two-mirror telescope, the beam reflects off the DM at an incidence angle of 8°. The beam then propagates approximately 2 m to a vacuum chamber, entering through an anti-reflection coated, 3 mm thick fused silica window. The beam is focused by a 2 in diameter, off-axis paraboloidal mirror with an angle of 60° and focal length of 7 cm.

Initial angular alignment of the paraboloid is performed by maximizing the brightness of a visible spark in ambient air. The pulse energy is reduced using filters and adjustment of the voltage on the final Pockels cell of the system until the spark is barely visible by eye. The mirror is then aligned to produce the brightest spark. Next, the pulse is further attenuated and the spark is again optimized. This process is repeated until no more optimization can be made.

The chamber is then filled with rarefied helium. A UV aluminum coated, 1 in diameter, $f/1$ off-axis paraboloidal mirror recollimates the focused beam. A dielectric mirror designed for broadband reflection at 800 nm is used before the collimating paraboloid to eliminate the fundamental light. Without this mirror, a significant second harmonic signal is generated on the surface of the aluminum paraboloid. An insignificant amount of surface second harmonic from the gold, focusing paraboloid was measured by temporarily placing the mirror before the focus.

The collimated beam is directed out of the chamber by a flat silver mirror through a 3 mm thick uncoated MgF_2 window. The beam is then focused by a 7.5 cm focal length doublet onto a small area silicon photodiode (Thorlabs DET210). A 3 mm thick B390 glass filter is placed before the recollimating paraboloid to further attenuate the fundamental light.

The impulse response of the photodiode is approximately 5 ns when terminated into 50 Ω. The photodiode signal is amplified and integrated by a triggerable boxcar device (Stanford Research Systems SR200). The boxcar output is digitized by a PC-based data acquisition device (National Instruments 6024E). The digitized signal is used as a figure of merit for a genetic algorithm that optimizes the DM figure [27].

The genetic algorithm iteratively searches for the optimum mirror figure by forming "generations" of figures from the best performing figures of the previous generation. In the runs described here, the algorithm produced 100 figures for each generation from the 10 best figures of the previous generation. Portions of each of the ten "parents" are randomly selected to construct each new figure. A small probability (usually 15% here) of random mutation of each new figure is imposed to supply new "genetic material" to each generation. The algorithm starts from a random figure,

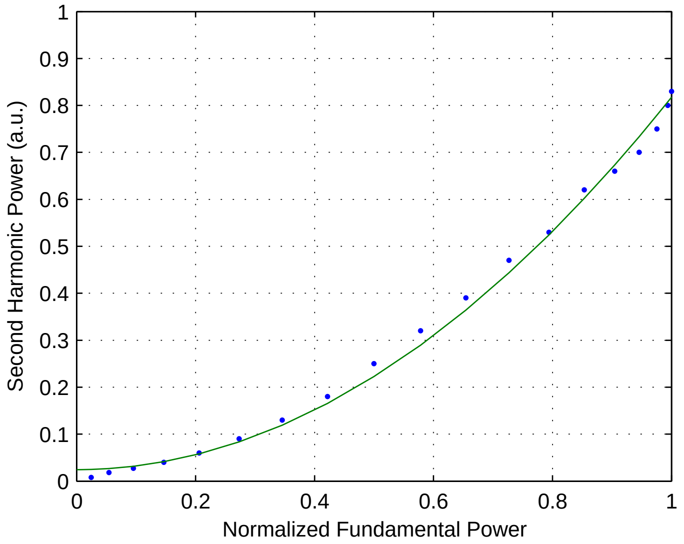

Figure 5.3: Second harmonic power versus incident power. Solid line shows the closest square law match.

a fixed figure (e.g. a constant voltage on all actuators), or a previously optimized figure.

The system was operated with a helium pressure of 4 Torr, which produced a photodiode signal of ∼200 mV when the signal was optimized. Fig. 5.4a shows the genetic improvement chart for a run starting with a random mirror figure. The improvement saturates after approximately 15 generations. Images of the focus were taken for two different DM figures: zero voltage on all actuators (Fig. 5.4b) and an optimized figure (Fig. 5.4c). The corrected focus has a higher peak intensity, better circularity and a larger fraction of the energy in the main spot. In order to verify that the signal was indeed second harmonic, energy scaling data was taken and shown to fit well to a square power law (Fig. 5.3).

5.3 Helium wavefront distortion

One of the purposes of performing high-intensity laser-plasma experiments in vacuum is to avoid self-phase modulation and other distortions due to the presence of

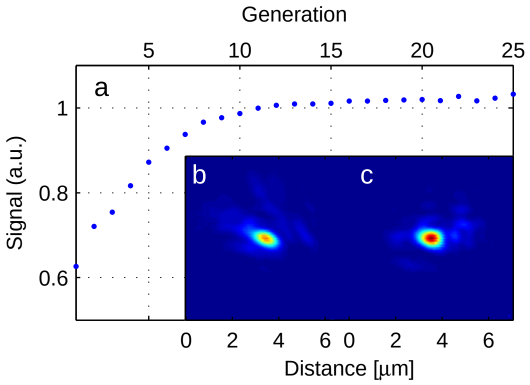

Figure 5.4: (a) Strength of the 2nd harmonic signal for the best child of each generation starting from a random mirror configuration. Inset: low power focus images for a flat mirror (b) and corrected mirror (c).

material (air) in the focusing beam. It is important then to determine what effect the presence of helium during the optimization process has. The amount of self-phase modulation can be determined by a simple B-integral calculation, where the B-integral is defined as

$$B(z) = \frac{2\pi}{\lambda} \int_{z_0}^{z} n_2 I(z) dz \tag{5.4}$$

In Eq. (5.4), n_2 is the nonlinear index of the medium and $I(z)$ is the spatially dependent intensity. Assume a Gaussian beam of the form

$$I(z,t,r) = I(z=0,t=0,r=0)\frac{w_0^2}{w^2(z)} e^{-2r^2/w^2(z)} e^{-4\ln 2t^2/\tau^2} \tag{5.5}$$

where w_0 is the $1/e^2$ focal spot size and τ is the FWHM pulse duration. For tightly focused beams, the Gaussian approximation is not strictly valid. However, experimentally, the focal intensity of the λ^3 system is overestimated by Gaussian beam calculations, so the B-integral estimated here represents an upper bound. Since we are only interested in the maximum amount of accumulated phase, which occurs on axis and at the peak of the pulse, we can reduce Eq. (5.5) to

$$I(z) = I(z, t=0, r=0) = I(z=0)\frac{w_0^2}{w^2(z)} = I_0\frac{w_0^2}{w^2(z)} \tag{5.6}$$

The beam size of a Gaussian is

$$w^2(z) = w_0^2(1 + z^2/z_{\mathrm{R}}^2) \tag{5.7}$$

where z_{R} is the Rayleigh range. Inserting Eq. (5.7) into Eq. (5.6) gives

$$I(z) = I_0\frac{1}{1 + z^2/z_{\mathrm{R}}^2} \tag{5.8}$$

The B-integral of Eq. (5.4) can now be performed:

$$\begin{aligned} B(z) &= \frac{2\pi}{\lambda}\int_{z_0}^{z} n_2 I_0 \frac{1}{1 + z^2/z_{\mathrm{R}}^2} dz && (5.9)\\ &= \frac{2\pi}{\lambda} n_2 I_0 z_{\mathrm{R}} \left[\tan^{-1} z/z_{\mathrm{R}}^2\right|_{z=0}^{z} && (5.10)\\ &= \frac{2\pi}{\lambda} n_2 I_0 z_{\mathrm{R}}[\tan^{-1} z/z_{\mathrm{R}}^2 - \tan^{-1} z_0/z_{\mathrm{R}}^2] && (5.11) \end{aligned}$$

Since we are interested in the phase accumulated from the focusing optic at $z_0 \gg z_{\mathrm{R}}$ to the focus at $z = 0$ we have

$$B(z) \approx \frac{2\pi}{\lambda} n_2 I_0 z_{\mathrm{R}} \left[0 - \left(-\frac{\pi}{2}\right)\right] = \frac{\pi^2}{\lambda} n_2 I_0 z_{\mathrm{R}} \tag{5.12}$$

Using the Gaussian beam relations $I_0 = 4E/(w_0^2 \tau \sqrt{\pi^3 \ln 2})$ and $f/\# = (\pi w_0)/2\lambda$ gives

$$B(z) = \frac{4E}{\lambda^2 \tau} n_2 \sqrt{\pi^3 / \ln 2} \tag{5.13}$$

The nonlinear index of helium at atmospheric pressure is 3.5×10^{-21} cm^2/W [31]. The index scales linearly with pressure, dropping by a factor of 190 at 4 Torr. Using parameters from the λ^3 system of E = 3 mJ, $\lambda = 800$ nm and $\tau = 30$ fs gives a net B-integral of 7.7×10^{-3} rad or approximately $\lambda/800$. Therefore, the nonlinear phase of helium at this pressure is negligible.

Another contributing factor is the linear plasma dispersion. Using the plasma dispersion relation:

$$k_p^2 c^2 = \omega^2 - \omega_p^2 \tag{5.14}$$

the linear phase is given by

$$\phi = k_p z = \frac{z}{c} \sqrt{\omega^2 - \omega_p^2} \tag{5.15}$$

Subtracting the phase of vacuum gives

$$\phi = k_p z - kz = \frac{z}{c}\left[\sqrt{\omega^2 - \omega_p^2} - \omega\right] \tag{5.16}$$

For the case of low pressure helium $\omega_p \ll \omega$ and Eq. (5.16) can be approximated as

$$\phi \approx \frac{z}{c}\left[\omega - \frac{1}{2}\omega_p - \omega\right] = \frac{z\omega_p}{2c} \tag{5.17}$$

Helium at 4 Torr has a density of $(2.5 \times 10^{19}\ \mathrm{cm}^{-3})(4\ \mathrm{Torr})/(760\ \mathrm{Torr}) = 1.3 \times 10^{17}\ \mathrm{cm}^{-3}$. Therefore, fully ionized helium at 4 Torr has an electron density of $n_e = 2.6 \times 10^{17}\ \mathrm{cm}^3$. This corresponds to a plasma frequency of 290 rad/ps. Double ionization of helium does not become significant until an intensity of $\sim 3\times10^{15}\ \mathrm{W/cm}^2$ [32]. For a 3 mJ, 30 fs pulse focused by an $f/1.4$ optic this intensity is achieved approximately 130 m before the focus. Using Eq. (5.17), the accumulated phase due to the helium plasma would be $\frac{z\omega_p}{2c} = \frac{(130\ \mathrm{m})(290\ \mathrm{rad/ps})}{2(300\ \mathrm{m/ps})} = 0.63$ rad, or approximately one tenth of a wave. In fact, the fraction of doubly ionized He is more than an order of magnitude lower than that of singly ionized He even at $10^{16}\ \mathrm{W/cm}^2$. Therefore, the majority of the propagation 130 um prior to focus occurs in a singly ionized He plasma with a plasma frequency of only 21 rad/ps leading to an accumulated phase of 0.44 rad, or $\sim \lambda/14$. This is smaller than the distortion one would expect from strongly attenuating filters and SPM.

The influence of SPM, plasma dispersion and other distorting effects (e.g. ionization blue-shifting) can be qualified by measuring their effect on the fundamental spectrum. To do this, the beam was collected by a paraboloidal mirror as in Fig. 5.2 without the high-reflector and directed out of the chamber. An integrating sphere was used to capture the entire beam, and a miniature spectrometer (Ocean Optics

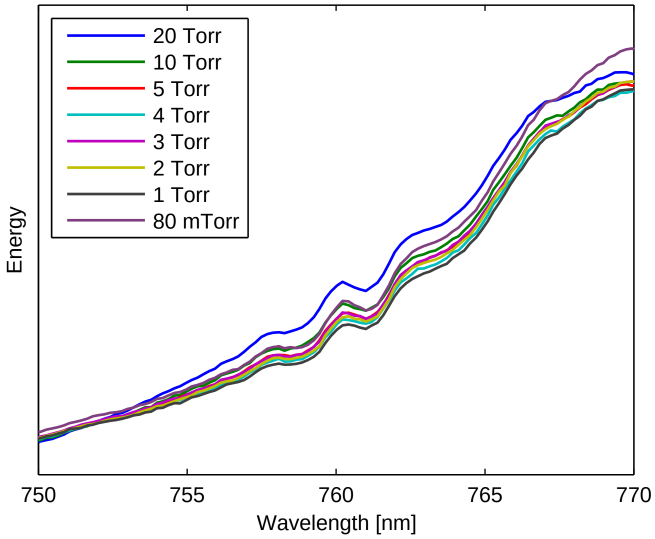

Figure 5.5: Fundamental spectra after focusing in various pressures of helium.

USB4000) measured the spectra at the output port of the sphere. The chamber was pumped down to 80 mTorr using only a rotary vane pump. The pump was then closed off and helium was leaked into the system, stopping to record a spectrum at several pressures up to 20 Torr. Each spectrum was integrated for 30 ms (15 laser shots) and averaged over 10 acquisitions, leading to a signal error of ∼2% due to uncertainty in the number of pulses collected.

As seen in Fig. 5.5, the spectra for all helium pressures < 10 Torr were indistinguishable within the stability of the spectrum. However, at 20 Torr a clear blue-shift in the range from 755 nm to 765 nm is visible. Since the optimization algorithm was performed at a pressure of only 4 Torr, and no detectable change in the spectrum occurs below 10 Torr, it is safe to say that the phase distortions introduced by the presence of helium are negligible.

5.4 Conclusion

In conclusion, a new method of optimizing the deformable mirror figure for high-intensity, high-NA experiments was presented. The primary advantage of the method is that it can be run with no attenuation, thereby correcting for all nonlinear and thermal aberrations present during normal operation and avoiding the aberrations introduced by attenuating filters. In addition, the optimization is not constrained to a fixed plane or dependent on fine alignment of diagnostics. This focal optimization method was successfully used in the high-harmonic experiment described in Chapter VI of this thesis.

In principle, this technique should be applicable to even higher intensity systems by further reducing the gas pressure. In such systems, the benefits of a full-power optimization method may be even greater, owing to the additional difficulty in attenuating beams in higher energy systems. For example, in multi-Joule systems, amplifiers must often be disabled to achieve sufficient attenuation.

This technique may also be implemented without the need for breaking vacuum between optimization and the experiment. The limited number of optics required to collect the second harmonic could be manipulated remotely. By maintaining vacuum, alignment errors caused by shifting of the optics during pressure changes (especially of the very sensitive paraboloidal mirrors) would be eliminated.

CHAPTER VI

High-order Harmonics

6.1 Introduction

The generation of ever shorter wavelengths of light is driven by a host of applications. In imaging, shorter wavelengths lead to higher spatial resolution. In studies of ultrafast dynamics, shorter wavelengths can be used to synthesize shorter duration pulses and achieve higher temporal resolution. In other applications, shorter wavelengths are of interest for their difference in absorption. For example, the so-called "water window" from 2.3 nm to 4.4 nm is a spectral region where the differential absorption between water and carbon allows high-contrast imaging of biological systems.

The main advantages of laser-based harmonic sources are their size and their ability to generate sub-femtosecond pulses. Synchrotrons are capable of producing very bright, short pulses, but require large facilities. Small, bright, continuum sources are available, but incapable of producing ultrashort pulses. Laser-based sources are a compromise. While not yet nearly as bright as synchrotrons, laser-based harmonic sources are compact and capable of producing sub-femtosecond pulses.

The generation of high-harmonics using gas targets is a maturing technology and has already been applied to many unique measurements. Unfortunately, the fundamental physics of harmonic generation in gases limits the driving intensity, and therefore the conversion efficiency. By moving to solid targets and employing different harmonic generation mechanisms, the intensity limit can be eliminated. High-order harmonics from high-intensity laser interactions with solid targets have the potential to produce coherent, high-brightness UV, and even x-ray, sources at higher conversion efficiencies than gas harmonics [33].

Here, the use of the term "harmonics" is mainly one of convenience and tradition. When discussing the generation of higher (or lower) energy radiation by perturbative processes in materials, the generation of harmonics is clearly understood. Multiple photons of the original wavelength (two for SHG, three for THG, etc.) are consumed to produce single photons of the new wavelength. These processes have a clear quantum mechanical nature.

Harmonic generation from solids is a very different process. While the fundamental laws of conservation of energy and momentum hold, the generation of harmonics cannot be regarded as simple whole number addition of fundamental photons. The harmonic nature of radiation from such experiments is due rather to the periodic nature of the driving radiation. The physical processes involved are repeated periodically during each cycle of the driving radiation. Fourier theory demands that a periodic signal must be composed of harmonics of the fundamental period. When the same processes occur only once, due to the use of single-cycle driving pulses for example, the generated radiation will not be found in the form of harmonics.

6.2 Harmonic generation mechanisms

Two dominant harmonic generation mechanisms in laser-solid interactions have been proposed and studied: coherent wake emission (CWE) [34] and the relativistic oscillating surface described by the oscillating mirror model (OMM) [35, 36]. Which of the two mechanisms is responsible for harmonic emission depends on the laser intensity and the plasma density scale-length. Roughly, CWE dominates for lower laser intensities ($a_0 < 1$) and shorter scale-lengths ($L < \lambda/2$), while OMM dominates for higher laser intensities ($a_0 > 1$) and longer scale-lengths ($L > \lambda/2$). Here, a_0 is the so-called normalized vector potential describing the intensity of laser-plasma interactions:

$$\begin{aligned} a_0 &= \sqrt{\frac{2e\lambda^2 I}{\pi m_e^2 c^5}} && (6.1) \\ &= 0.86 \times 10^{-9} I^{1/2}\ [\mathrm{W/cm^2}] && (6.2) \end{aligned}$$

6.2.1 Coherent wake emission

In coherent wake emission, electrons driven into the overdense plasma form plasma wakes that match the momentum of harmonics leaving the plasma and can therefore coherently amplify optical waves [34]. The limiting frequency in CWE is the plasma frequency of the target, because the turning point of an optical wave in a plasma, where the phase matching occurs, is near the critical density. Unfortunately, because the plasma does not have a step-like density profile, each harmonic is generated at different depth (deeper for higher orders), leading to a positive chirp of the spectrum. It is believed that CWE requires a short scale-length so that the electrons causing the wake can be driven deeply enough into the plasma [37].

6.2.2 Oscillating mirror model

In the oscillating mirror model, harmonic emission is a result of Doppler upshifting of the incident radiation reflected off the oscillating critical surface. The periodic motion of the critical surface, driven by the incident radiation itself, alternately stretches and compresses the light which is reflected off the surface. If the motion of the surface is described by $x(t) = d_1 \sin(\omega t) + d_2 \sin(2\omega t)$ then the phase shift of the reflected wave is

$$\phi(t) = 2\frac{x(t)\cos\theta}{\lambda} = 2\frac{\cos\theta}{\lambda}(d_1\sin(\omega t) + d_2\sin(2\omega t) \tag{6.3}$$

where θ is the angle of incidence. The component at 2ω is due to the $\mathbf{v}\times\mathbf{B}$ force, which, being the product of two components at ω, occurs at twice the frequency. The field of the reflected wave is

$$E_r(t) \propto e^{i\omega t}e^{i\phi(t)} \tag{6.4}$$

Since $e^{i\omega t}$ and $e^{i\phi(t)}$ are both periodic with frequency ω, the spectrum of the reflected field must be composed of harmonics of ω. The Fourier transform of Eq. (6.4) is

$$\begin{aligned}
E_r(\Omega) &\propto \mathcal{F}\left\{e^{i\omega t}e^{i2d_1\cos\theta\sin\omega t/\lambda}e^{i2d_2\cos\theta\sin 2\omega t/\lambda}\right\} && (6.5)\\
&= \delta(\Omega-\omega) * \mathcal{F}\left\{e^{i2d_1\cos\theta\sin\omega t/\lambda}\right\} * \left\{e^{i2d_2\cos\theta\sin 2\omega t/\lambda}\right\} && (6.6)\\
&= \delta(\Omega-\omega) * \sum_{p=-\infty}^{\infty} J_p\left(\frac{2d_1\cos\theta}{\lambda}\right)\delta(\Omega-p\omega) * \sum_{q=-\infty}^{\infty} J_q\left(\frac{2d_2\cos\theta}{\lambda}\right)\delta(\Omega-2q\omega) && (6.7)\\
&= \sum_{p=-\infty}^{\infty}\sum_{q=-\infty}^{\infty} J_p\left(\frac{2d_1\cos\theta}{\lambda}\right) J_q\left(\frac{2d_2\cos\theta}{\lambda}\right)\delta(\Omega-(p+2q+1)\omega) && (6.8)
\end{aligned}$$

If $d_1 = 0$ (i.e. no fundamental motion of the critical surface) then the first Bessel function is nonzero only for $p = 0$ and only odd harmonics, $(2q+1)\omega$, are allowed. If $d_2 = 0$ (i.e. no $\mathbf{v}\times\mathbf{B}$ motion of the critical surface) then the second Bessel function is nonzero only for $q = 0$ but all harmonics $(p+1)\omega$ are still allowed. Eq. (6.8) describes the dependence of harmonic order on the frequency of the critical surface motion. It does not however describe the correct amplitudes of the harmonics. The reason is that Eqs. (6.3) and (6.4) are not self-consistent. Since the total field at the surface is the sum of the incident and reflected fields, the reflected field also plays a role in the motion of the surface. More rigorous theories account for this effect and predict more accurate conversion efficiencies [36, 38].

Selection rules can be derived for the existence of even- and odd-order harmonics as a function of incident polarization [38]. Table 6.1 shows these selection rules for linear, oblique incidence.

Driving Polarization	Harmonic Polarization	
	Odd	Even
P	P	P
S	S	P

Table 6.1: Selection rules for the polarization of OMM harmonics for given driving polarizations.

The reason for the selection rules is that there are two oscillation components of the critical surface: a fundamental component due to the driving electric field and a second harmonic component due to the $\mathbf{v} \times \mathbf{B}$ force. There are also two forms of radiation: the upshifted, reflected light (which will have the same polarization as the incident light) and the light radiated by the surface itself (which will be P-polarized). For P-polarized driving, the surface oscillates at both ω and 2ω, radiating both odd and even P-polarized light. The reflected light (P-polarized) is modulated at both ω and 2ω, and therefore contains both odd and even harmonics as well. For S-polarized driving, the surface oscillates only at 2ω, radiating even order P-polarized light. The reflected light (S-polarized) is modulated at 2ω, and therefore contains only odd harmonics ($\omega + 2\omega$, $\omega + 4\omega$, ...).

6.2.3 Scale-length dependence

One of the most important characterizations of the target interface is its density profile at the time of the arrival of the main pulse. In practice, the density profile could be a very complex function falling from solid density in the unaffected region of the plasma to vacuum. In most theoretical and numerical models of laser-solid interactions, however, the plasma is assumed to have a simple profile (e.g. linear or exponential) with a characteristic scale-length, often defined as

$$L = n\left(\frac{dn}{dz}\right)^2 \tag{6.9}$$

For an exponential profile, $n = n_0 exp(\alpha z)$, this gives the convenient result:

$$L = n_0 e^{\alpha z}(n_0 \alpha e^{\alpha z})^{-1} = \alpha^{-1} \tag{6.10}$$

It is generally agreed that a sharp plasma profile (usually $< \lambda/2$) is necessary for efficient generation of harmonics with good spatial coherence. In experiments with long-pulse lasers (on the order of 1 ps or longer) it has been shown that the ponderomotive pressure of the laser is able to steepen an initially long scale-length to the necessary scale-length for efficient high-harmonic production [39]. However, femtosecond scale pulses are too short to cause considerable profile steepening during their duration. Therefore, the scale-length must be kept short prior to the arrival of the pulse. This requires sufficiently low prepulse and ASE energy and intensity in the leading edge of the pulse.

Whether there is an optimum scale length is still a matter of debate. Most experimental data have demonstrated monotonically decreasing conversion efficiency with scale length [40]. However, some simulations have predicted that an optimal scale length exists [37]. In addition, 2D PIC simulations have shown an optimum target density of $n = a_0 n_{\mathrm{cr}}/2$ [41].

6.2.4 Calculating scale-length

Physically measuring a sub-micron scale-length is a daunting task. Visible wavelength probing does not have the resolution to distinguish the desired features [42,43]. X-ray wavelengths can be used, but the spatial coherence of x-ray sources is not high enough to support better resolution than visible probes. In the literature, scale-lengths are generally simulated from hydrodynamic codes (e.g. HYADES [44,45]) or calculated based on self-similar plasma expansion at the ion sound speed:

$$c_s = \sqrt{\frac{\gamma Z * kT_e}{m_i}} \tag{6.11}$$

where the ionization number, $Z*$, and the electron temperature, T_e, are estimated from other measurements or calculations.

6.3 λ^3 and high-harmonics

The λ^3 regime was described in the introduction of the thesis. Some of the unique properties associated with high-NA focusing and their possible effects on harmonic generation are worth mentioning here.

6.3.1 Longitudinal field component

In a tightly focused beam ($w_0 \approx \lambda$) strong longitudinal electric fields are present at focus [46]. The first order correction to the Gaussian beam formulation states that the longitudinal component is proportional to the square of the divergence angle

($E_z \propto \theta^2$) [47, 48]. However, the first-order correction works accurately only up to a few degrees. Higher-order correction terms can be added, but the number of necessary terms becomes asymptotically large in the limit of tightly focused beams ($w_0 \approx \lambda$) and different formulations become necessary [49]. If this longitudinal field is sufficiently strong then it will directly drive electrons in the same direction as the $\mathbf{v} \times \mathbf{B}$ force. In contrast to the $\mathbf{v} \times \mathbf{B}$ force, a longitudinal field will oscillate at the fundamental frequency, generating all orders of P-polarized harmonics. P-polarized driving already leads to P-polarized harmonics of all orders, however, the odd harmonics due to S-polarized driving are S-polarized. A longitudinal field would therefore contribute additional harmonics to S-polarized driving.

6.3.2 Large divergence

Because the divergence angle of an $f/1$ optic is $\sim 45°$ the divergence angle of the harmonics might also be large. The simplest method of estimating the harmonic divergence is to assume that the source size is equal to the focal size of the driving beam and that the wavefront is flat. Gaussian beam theory then gives a divergence angle of

$$\theta_n = \frac{\lambda_n}{\pi w_0} \tag{6.12}$$

In the case of harmonics, $\lambda_n = \lambda/n$ and Eq. (6.12) can be written as

$$\theta_n = \frac{\lambda/n}{\pi w_0} = \frac{\theta}{n} \tag{6.13}$$

where θ is the fundamental divergence angle. This type of divergence has not in fact been observed. One possible explanation is that the ponderomotive force of the driving pulse dents the target surface, modifying the divergence properties of the harmonics [50, 51].

6.3.3 Spatial gradients

In many simulations the incident electromagnetic field is taken to be planar or nearly planar, simplifying the interaction. In many experimental cases this approximation is valid given that the focal spot size is many times larger than the wavelength ($w_0 \gg \lambda$). However, for a tightly focused beam ($w_0 \approx \lambda$) the plane wave approximation no longer holds and the significant, transverse, spatial gradients can play a role in the interaction. In extreme cases, the spatial gradients have led to the production of attosecond pulses that are emitted in completely different directions during different cycles of the driving pulse [52].

6.4 Experiment

The experiment was performed on the λ^3 laser system at the University of Michigan, described in the first chapter of this thesis. A diagram of the experiment is shown in Fig. 6.1.

Wavefront corrected, 50 fs, 2 mJ pulses are focused onto a bulk target by an $f/1.4$ off-axis paraboloid (OAP). The measured focal spot size was 1.7 μm (FWMH), producing an intensity of 1.1×10^{18} W/cm^2. For most of the shots, the target material was polished fused silica, however other types of glass and metals were also used. The P-polarized beam was incident on the target at 35°. This angle was chosen mostly due to constraints set by the necessary proximity and angle of the grating. The target was held by a motorized, three-axis translation stage which allowed the target to be positioned at focus and raster scanned to expose fresh surface for each shot. A shot separation of 100 μm was found to be sufficient for reliable operation. The specular beam was collected by an iridium coated, 1200 grooves/mm, spherical grating

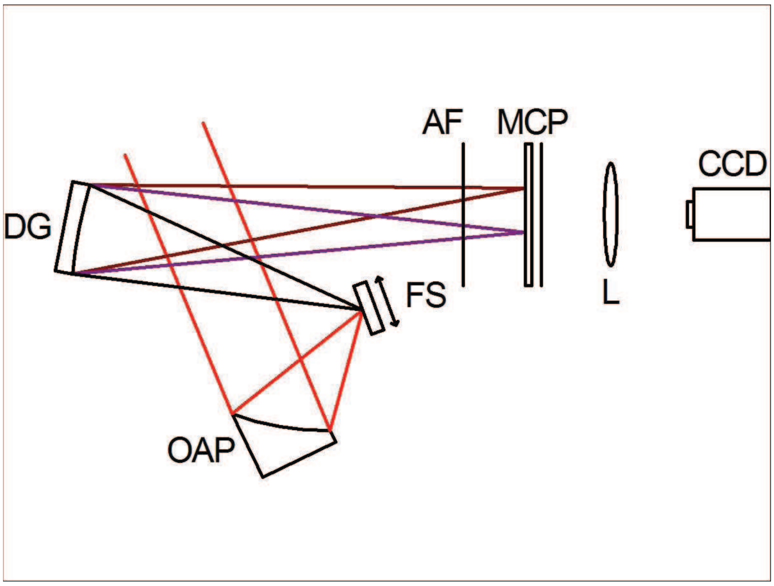

Figure 6.1: Diagram of the high-harmonic experiment. OAP: gold-coated, f/1.4, off-axis paraboloidal mirror; FS: fused silica target; DG: iridium-coated, 1200 grooves/mm diffraction grating; AF: 650 nm aluminum filter; MCP: phosphor-backed microchannel plate; L: zoom lens.

(Princeton Instruments 02-120H-03) which dispersed the spectrum across the surface of a microchannel plate (MCP). The incidence angle on the grating was either 5° or 6° depending on which spectral range was being observed. The specifications of the MCP are shown in Table 6.2.

Active diameter	75 mm
Enhancement coating	none
Maximum operating voltage	2.4 kV
Number of plates	2 (chevron configuration)
Phosphor	P20
Maximum phosphor voltage	5 kV

Table 6.2: Specifications of the MCP (Photonis 75/32/25/8 I 40:1).

The MCP was sufficiently insensitive to the fundamental light that no filter was necessary. However, a 650 nm thick aluminum filter was often used to block lower order harmonics and reduce the noise due to charged particles. A standard machine vision CCD camera and zoom lens were used to record the signal from the phosphor. Ray-tracing (ZEMAX) and CAD software were used to determine the geometry of all the components. Tolerances on the position and rotation of the grating were sufficiently large to allow it to be installed by hand with no need for remote manipulation during experiments. The chamber was evacuated by a turbo-molecular pump to pressures below 10^{-5} mbar in order to allow safe operation of the MCP.

While the λ^3 system is capable of operating at 500 Hz, the geometry of the vacuum chamber required the use of a target manipulator that could not be operated at high repetition rates. However, with an appropriate vacuum chamber no fundamental obstacles prevent the use of a target manipulator compatible with multi-kilohertz repetition rates. Many other solid target experiments have been successfully conducted on the λ^3 system at its full 500 Hz operation rate.

6.4.1 MCP gain

The MCP was operated primarily between 0.9 kV and 1.4 kV, however, the only published gain value was 4×10^6 at 2 kV. A mercury lamp was used to illuminate the MCP at various voltages. The lamp was placed outside of the chamber, visible to the MCP through a 3 mm thick fused silica window. Images of the MCP phosphor were acquired and integrated for several different values of MCP voltage (Table 6.3). The phosphor voltage was held at 5 kV for every acquisition. At the higher voltage values the MCP current was measured with a nanoammeter. The MCP has a dark current of approximately 20–30 μA in this voltage range. However, the nanoammeter was capable of offsetting the dark current and measuring only the difference in current as the mercury lamp was switched on and off. The differential currents for the three highest voltages used (1.4, 1.5, and 1.6 kV) were 0.1, 0.4, and 1.2 μA, respectively.

The current values were used for two purposes. The first was to approximate the gain of the MCP. A manufacturer specified gain was only available at only one point: 4×10^6 at 2 kV. In order to determine the gain at lower voltage where the MCP was operated, a power scaling was used [53]:

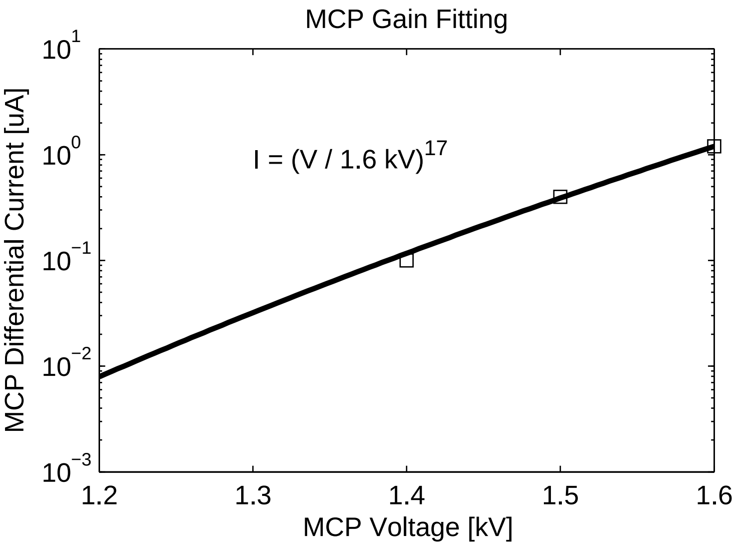

Figure 6.2: Power law fit to the measured MCP currents at 1.4, 1.5, and 1.6 kV during illumination by a mercury lamp.

$$G = (V/V_c)^m \tag{6.14}$$

V_c represents the voltage at which electron amplification and loss are balanced, resulting in no net gain. From Eq. (6.14), the MCP current is simply

$$I = I_0 G = I_0 (V/V_c)^m \tag{6.15}$$

where I_0 is the rate of charge production (a current) produced at the front of the MCP (via photoionization by the mercury lamp or by harmonics). Fig. 6.2 shows a fit using the three measured current values and extrapolation of the gain to lower voltages.

The values were fit to a function of the form $I' = (V'/V_c')^m$ where the primed values are dimensionless: $I = I'(1\ \text{kV})$, $V = V'(1\ \mu\text{A})$, and $I_0/V_c^m = (1/V_c')^m$. The fitting parameters were $m = 17.5$ and $V_c\prime = 1.58$. Extrapolating to 2 kV gives a current of 59 μA. Because the gain is known to be 4×10^6 at 2 kV, the current at the front of the MCP can be calculated from Eq. (6.15) as

$$I_0 = I/G = 59\ \mu\text{A}/4 \times 10^6 = 15\ \text{pA} \tag{6.16}$$

Since the illumination was unchanged for all of the data shown in Table 6.3, the initial current, $I_0 = 15$ pA, is also unchanged. A response value for the combination of MCP and camera can be therefore be calculated. The total charge that passed through the MCP for each acquisition was calculated by multiplying the initial current by the integration time of the camera (Table 6.3, column 6). The integration time had to be increased as the voltage was lowered to maintain a measurable signal. The number of counts from each image was then obtained and normalized by the setting of the camera gain (Table 6.3, column 5). Dividing these two values gives a response in counts/pC (Table 6.3, column 7).

Voltage [kV]	Phosphor Voltage [kV]	Integration Time [ms]	Camera Gain	Counts	Charge [pC]	Response [counts/pC]
1.6	5	5.48	3.29	2.8×10^8	0.11	2.6×10^9
1.5	5	5.48	3.29	1.5×10^8	0.11	1.4×10^9
1.4	5	32.4	3.29	3.3×10^8	0.65	5.2×10^8
1.3	5	93	3.29	3.3×10^8	1.9	1.8×10^9
1.2	5	305	3.29	2.9×10^8	6.1	4.8×10^7
1.1	5	950	3.29	2.1×10^8	19	1.1×10^7
1.0	5	2460	3.29	1.1×10^8	49	2.3×10^6
0.9	5	11700	3.29	1.3×10^8	230	5.5×10^5

Table 6.3: MCP calibration data. The number of counts is scaled to the number that would be expected for a gain of 1. The charge is found by multiplying the known current (15 pA) by the integration time.

6.4.2 Grating efficiency

The grating used for this experiment (Princeton Instruments 02-120H-03, Table 4) was removed from a commercial EUV monochromator (Acton VM-502).

Dimensions	40 mm × 45 mm
Radius of curvature	224.1 mm
Groove density	1200 mm^{-1}
Groove type	Unblazed holographic
Modulation depth	Very low (44 nm, estimate)
Coating	Iridium
Intended wavelength range	100 nm – 200 nm

Table 6.4: Diffraction grating specifications.

Information on the diffraction efficiency (both relative and absolute) of the grating was unavailable despite requests to the manufacturer. However, it was known that the modulation depth was very low, which is typical for EUV gratings. It was also known that the maximum diffraction efficiency occurred at approximately 150 nm. The diffraction efficiency of very low modulation depth gratings is accurately modeled by simple scalar diffraction theory [54], with the maximum diffraction efficiency occuring at

$$\lambda_B = 3.4h \tag{6.17}$$

where h is the peak-to-valley modulation depth.

Scalar diffraction theory calculates the efficiency by simply Fourier transforming the transfer function of the grating (i.e. Fraunhoffer diffraction) [55]. The transfer function of a sinusoidal phase grating is

$$T = \exp\left[i\frac{h}{2}\sin(2\pi Nx)\right] \tag{6.18}$$

Fourier transforming yields

$$\mathcal{F}\{T\} = \sum_{m=-\infty}^{\infty} J_m(\frac{2\pi h}{\lambda})\delta(f_x - mN) \tag{6.19}$$

The sum in Eq. (6.19) is over the various diffraction orders represented by the same variable, m, in the grating equation $\sin\gamma - \sin\theta = m\lambda N$. The delta function is simply an expression of the grating equation, where the transform variable f_x is related to the diffraction angle. The efficiency is found by squaring Eq. (6.19):

$$\left[\sum_{m=-\infty}^{\infty} J_m\left(\frac{2\pi h}{\lambda}\right)\delta(f_x - qN)\right]^2 = \sum_{m=-\infty}^{\infty} J_m^2\left(\frac{2\pi h}{\lambda}\right)\delta^2(f_x - mN) \tag{6.20}$$

Pulling the square inside the sum of Eq. (6.20) is allowed because the delta functions prevent the orders from overlapping. In the case of a finite grating, the delta functions are replaced by other functions (sinc functions for a square grating), but as long as the orders are sufficiently spaced (which they are in most practical situations) Eq. (6.20) is still valid.

Using the optimum diffraction wavelength of 150 nm in Eq. (6.17) gives a peak-to-valley modulation depth of h = 150 nm/3.4 = 44 nm. Fig. 6.3 shows a plot of Eq. (6.20) for this modulation depth.

The most striking feature of the theoretical diffraction efficiency is the presence of nulls at 72 nm, 39 nm, 27 nm, and so on. The efficiency drop around 72 nm is clearly visible in the experimental spectrum (Fig. 6.4) between harmonics 10 and 11. The fact that the 11th harmonic should fall almost exactly on the null (800 nm/11 = 72.7 nm) but is still visible can be attributed to several factors: (i) the broad bandwidth of the laser and the central wavelength being closer to 790 nm than 800 nm; (ii) imperfections in the ruling of the grating, which effectively smooth the efficiency

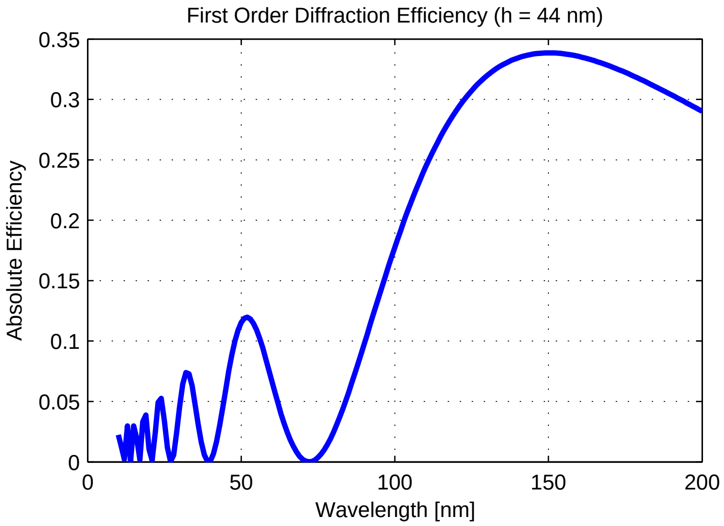

Figure 6.3: Theoretical first-order ($m = 1$) absolute diffraction efficiency for a modulation depth of 44 nm.

curve and eliminate the nulls; (iii) the wavelength of maximum diffraction efficiency is not exactly known. The third peak in diffraction efficiency around 32 nm is also visible in the experimental spectrum.

6.5 Analysis

An example of spectral data acquired during this experiment is shown in Fig. 6.4. Harmonics up to the 18th are detectable. Wavelengths below the 11th harmonic are blocked by an aluminum filter. The grating efficiency, described earlier, limits detection above the 18th harmonic. A small amount of emission with no observable harmonic structure is visible in the image and lineout from approximately 28 nm to 35 nm.

Lower order spectra were also taken (Fig. 6.5) by using the grating at a 5° incidence angle rather than 6° and removing the aluminum filter. The divergence of these harmonics is much larger than those of the higher orders in Fig. 6.4. The reason for this is that the lower order harmonic data was acquired first, before an optimum

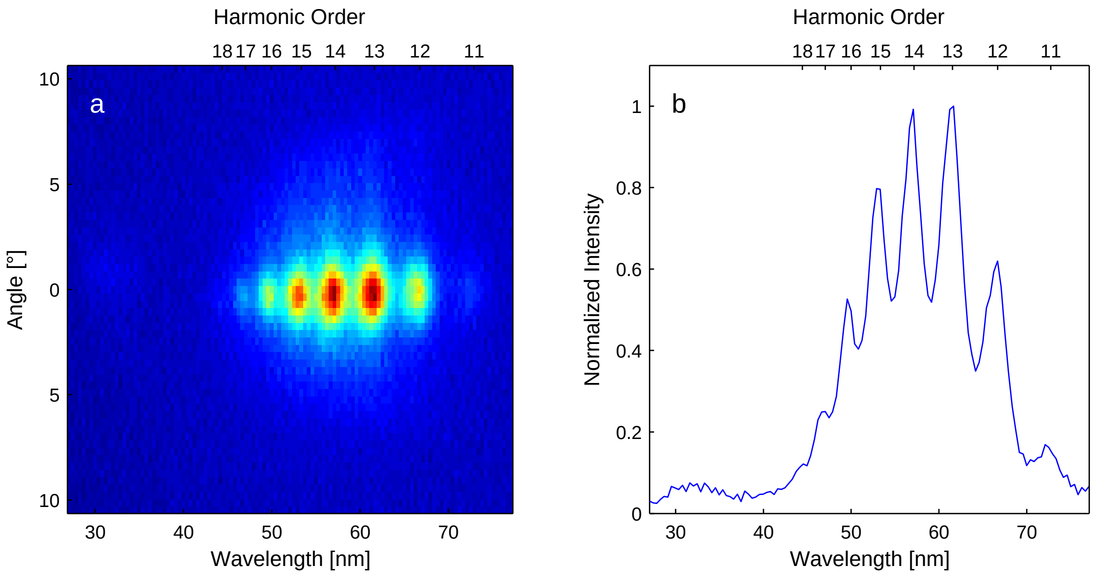

Figure 6.4: Raw phosphor image (a) and lineout (b) showing harmonics 11 through 18.

target alignment procedure was determined. The relationship between target position and divergence angle is discussed later in this chapter.

6.5.1 Conversion efficiency

The MCP response values from Table 6.3 were used to determine the number of photoelectrons produced by each harmonic from the experimental images. Table 6.5 shows the number of counts for each harmonic based on the image in Fig. 6.4. Ta-

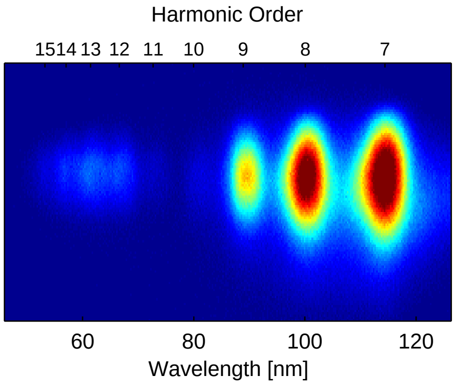

Figure 6.5: Lower order harmonics measured with no aluminum filter.

ble 6.5 also lists the quantum efficiency (QE) of the MCP, the reflectivity of iridium, the diffraction efficiency of the grating, and the transmission of the aluminum filter. Dividing by all of these values yields a total number of photons produced by the source for each harmonic (6.6). The wavelengths, photon energies, total energy, and efficiency for each harmonic (based on an input energy of 2 mJ) are also shown in Table 6.6.

Harmonic Order	Photoelectron Count	MCP QE	Iridium Reflectivity	Diffraction Efficiency	650 nm Al Transmission
13	2.9×10^4	0.1	0.20	0.048	0.22
14	5.9×10^4	0.1	0.21	0.094	0.23
15	5.2×10^4	0.1	0.21	0.12	0.24
16	3.4×10^4	0.1	0.20	0.12	0.22
17	1.4×10^4	0.1	0.17	0.089	0.21
18	4.3×10^3	0.1	0.15	0.045	0.21

Table 6.5: Photoelectron count detection parameters for harmonics 14–18.

Harmonic Order	Wavelength [nm]	Photon Energy [eV]	Photons	Total Energy [pJ]	Efficiency
13	61	20	1.4×10^8	440	2.2×10^{-7}
14	57	22	1.3×10^8	450	2.2×10^{-7}
15	53	23	8.5×10^7	320	1.6×10^{-7}
16	50	25	6.4×10^7	250	1.2×10^{-7}
17	47	26	4.3×10^7	180	9.1×10^{-8}
18	44	28	3.0×10^7	130	6.8×10^{-8}

Table 6.6: Calculations for the efficiency of each harmonic. An input energy of 2 mJ was used to calculate the efficiencies.

The conversion efficiencies were fit to a power law (Fig. 6.6). This scaling is consistent with that reported by Norreys [56] using high-energy picoseconds pulses, where the exponent of the fit ranged from -5.5 at $I\lambda^2 = 5 \times 10^{17}$ W μm^2 cm^{-2} to -3.4 at $I\lambda^2 = 1.0 \times 10^{19}$ W μm^2 cm^{-2}. The absolute conversion efficiency is also comparable, with Norreys reporting efficiencies between 10^{-6} and 10^{-7} above the 14th harmonic. It should be noted that those results assumed isotropic emission, whereas the harmonics described in this thesis are emitted as beams.

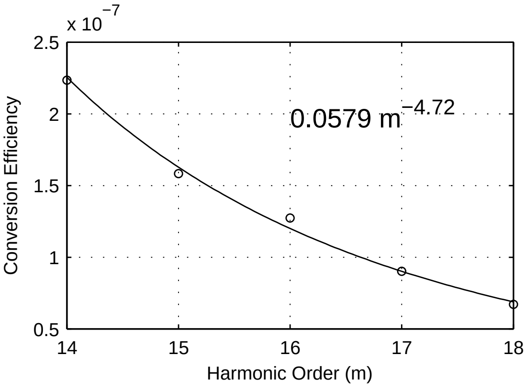

Figure 6.6: Conversion efficiencies for harmonics 14 through 18 (circles) and power law fit (solid line).

Solid target harmonic PIC simulations performed by Gibbon [57] predicted an efficiency scaling of

$$\eta = 9 \times 10^{-5} \left(\frac{I\lambda^2}{10^{18}\ \mathrm{W}\,\mu\mathrm{m}^2\,\mathrm{cm}^{-2}} \right)^2 \left(\frac{m}{10} \right)^{-5} \tag{6.21}$$

The dependence on harmonic order (m^{-5}) is similar to that in Fig. 6.6, however, the efficiencies reported by Gibbon are approximately an order of magnitude higher. Simulations using the 2D PIC code OSIRIS [58] were performed for the λ^3 experimental parameters with a scale-length of $\lambda/4$. The harmonic power is shown in Fig. 6.7. The efficiency of harmonics 13 through 19 scale as $n^{-5.3}$, simliar to the experiment, though the absolute efficiency is approximately 40 times higher.

Absolute efficiency can be affected by a number of factors. Target surface roughness and wavefront distortion of the driving beam can cause harmonic energy to be scattered outside the collection angle. Fundamental energy can also be scattered outside of the main focus by wavefront errors and roughness of the paraboloid. Finally, the calibration of the MCP is imprecise and its gain could be lower than specified, especially due to age.

The total conversion efficiency into all measurable harmonics passed by the alu-

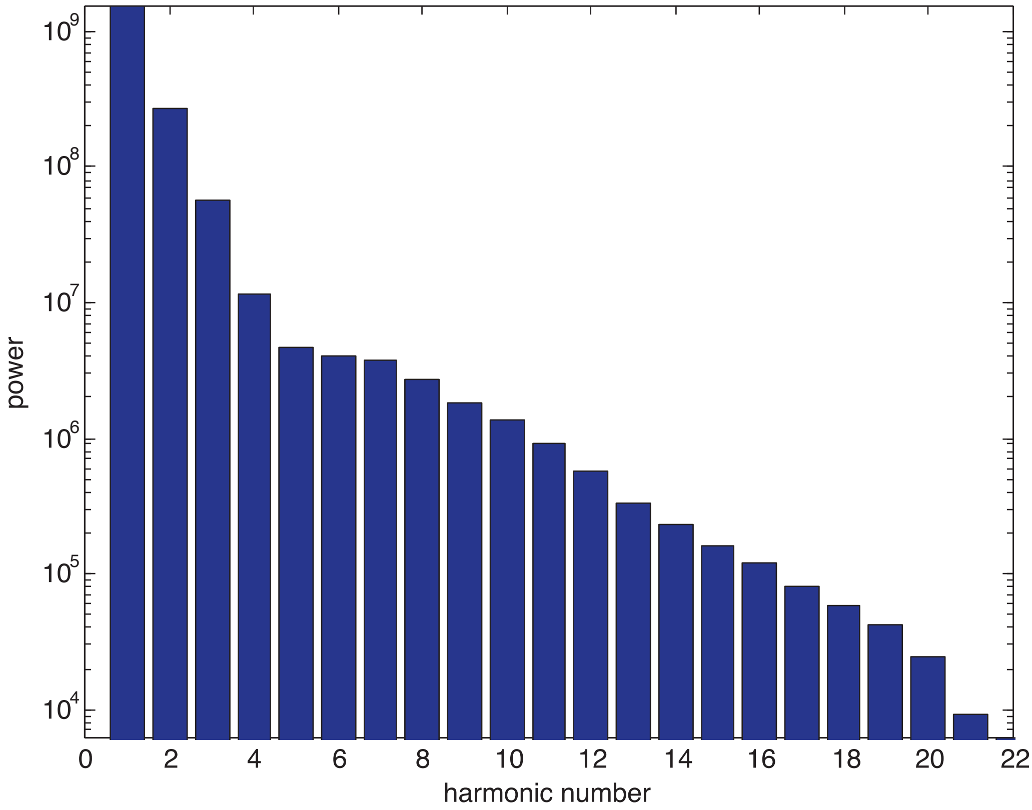

Figure 6.7: Harmonic power from 2D PIC simulations for the λ^3 parameters with a scale-length of $\lambda/4$.

minum filter was 8.9×10^{-7}. This value is comparable to those reported from recent gas harmonic experiments [59,60]. However, solid target experiments should be scalable to much higher intensities. State-of-the-art CPA systems operating at kilohertz repetition rates can now produce sub-30 fs pulses with 10 mJ - 20 mJ of energy. Focusing such pulses to the diffraction limit would yield intensities of $> 10^{19}$ W/cm^2. At such intensities, the harmonic conversion efficiency should be significantly higher. At 10^{20} W/cm^2, conversion efficiencies above 10^{-5} per harmonic have been estimated around 17 nm [61].

6.5.2 Intensity scaling

Harmonic spectra were recorded with different driving pulse energies to determine the scaling of efficiency with intensity. Fig. 6.8 shows the integrated harmonic energy of harmonics 12 through 18 at laser intensities from 5×10^{17} W/cm^2 to 1×10^{18} W/cm^2. Also plotted are the experimentally observed $I^{0.4}$ scaling law of CWE harmonics from Quere et al. at $I\lambda^2 \approx 10^{16}\ \mathrm{W}\,\mu\mathrm{m}^2\,\mathrm{cm}^{-2}$ [34] and the I^2 scaling law observed in PIC simulations by Gibbon for $I\lambda^2 \approx 10^{18}\ \mathrm{W}\,\mu\mathrm{m}^2\,\mathrm{cm}^2$ [57]. Shot-to-shot variations in harmonic energy were substantial, most likely due to timing jitter that occurs when the Pockels cell voltage is changed, but the data suggests a slightly sublinear intensity scaling, closer to that of the experimental CWE harmonics.

The best fit power law scaling to the data is $I^{0.64}$. By increasing the intensity of a λ^3 style system to 10^{19} W/cm^2, this scaling predicts a combined conversion efficiency of 4×10^{-6}. In fact, above 10^{18} W/cm^2, as relativistic effects begin to play a greater role than CWE, the scaling law should move toward that of I^2. Further increasing the intensity to 10^{20} W/cm^2, not inconceivable in a λ^3 system, could potentially provide another 100-fold increase in conversion efficiency.

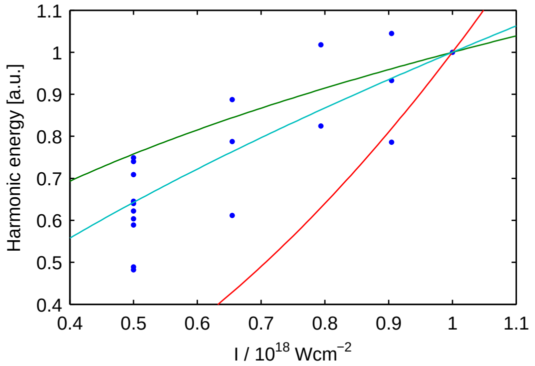

Figure 6.8: Harmonic intensity scaling. Blue dots: integrated energy of harmonics 12 through 18 at laser intensities from 5×10^{17} W/cm^2 to 1×10^{18} W/cm^2. Green line: $I^{0.4}$ scaling experimentally observed by Quere for $I\lambda^2 \approx 10^{16}$ W μm^{2}cm^{-2} [34]. Red line: I^2 scaling predicted in PIC simulations by Gibbon for $I\lambda^2 \approx 10^{18}$ W μm^2 cm^{-1} [57]. Blue line: $I^{0.64}$ best fit.

6.5.3 Divergence

Because the diffraction grating was used off-normal, astigmatism separated the vertical and horizontal foci. To achieve the highest spectral resolution, the MCP was positioned at the horizontal focus. This left the MCP sufficiently far from the vertical focus to be in the realm of geometric optics for that dimension. That is, the vertical dimension on the MCP maps directly to angles from the source.

When poor focusing conditions generated highly divergent harmonics, the boundaries of the diffraction grating became visible in the acquired images. This provided a simple method of calibrating the spatial to angular mapping. The boundaries are somewhat visible in the spectrum of Fig. 6.5 and more pronounced in a later figure (Fig. 6.13). The height of the grating was 40 mm, so that at a distance of 14.6 cm the full vertical collection angle of the grating was 15.3°.

Table 6.12 lists the divergence data for harmonics 13 through 16, those with sufficient signal to accurately measure their divergence. Taking the anomalously small divergence of the 13th harmonic to be a result of measurement uncertainty, all of the measurable orders had similar divergence angles, with a slight trend toward higher divergence for higher harmonics.

Harmonic order	Divergence [pixels]	Full grating divergence [pixels]	Divergence [deg]
12	9 ± 1	43 ± 2	3.3 ± 0.5
13	8 ± 1	45 ± 2	2.8 ± 0.5
14	9 ± 1	39 ± 2	3.6 ± 0.4
15	8 ± 1	35 ± 2	3.6 ± 0.6
16	8 ± 1	28 ± 2	4.5 ± 0.7

Table 6.7: Harmonic Divergence

The increasing divergence angles are inconsistent with the simple argument made in the introduction that the harmonics would diverge with angles $\theta_n = \theta/n$. Denting of the target could be responsible for modifying the divergence angles, especially with the strong spatial gradients in the λ^3 regime. But, a simpler explanation is that the shorter wavelength, higher order harmonics are more sensitive to surface roughness and imhomogeneities of the plasma, leading to poorer wavefront quality and higher divergence. Higher resolution data from a larger number of harmonics is necessary to further understand this phenomenon.

2D PIC simulations of the interaction reproduce the measured divergence angle. A 2D spatial Fourier transform of the reflected field is shown in Fig. 6.9. The angular profile of the 15th harmonic is shown in Fig. 6.10. The FWHM divergence angle is 3.6°, which agrees very well with the measured divergence.

6.5.4 Polarization dependence

The effect of driving polarization was also measured. Zero-order mica waveplates were used to generate S- and circular polarization. Mica is used because single sheets of acceptable quality can be obtained by peeling from large crystals. When dealing with high-power and ultrashort pulses, thin mica sheets are preferable to traditional zero-order waveplates of much greater thickness.

The harmonic behavior of S-polarized driving light was tested by using a half-

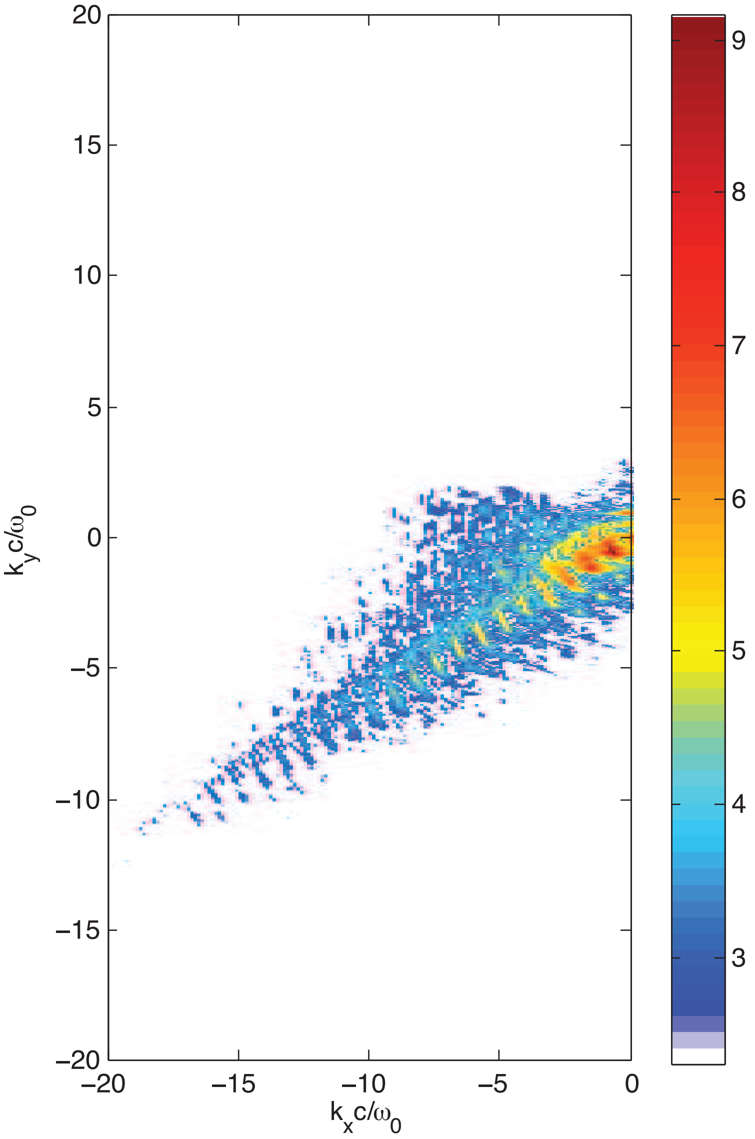

Figure 6.9: 2D spatial Fourier transform of the reflected beam from 2D PIC simulation.

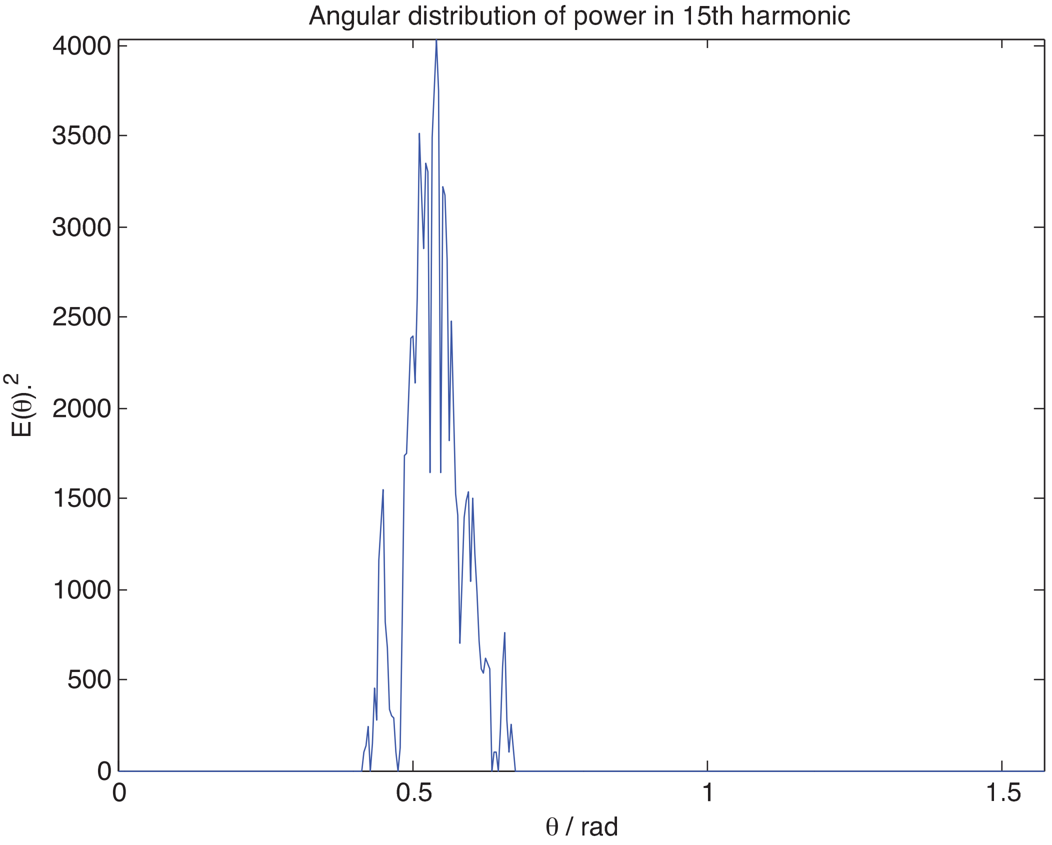

Figure 6.10: Angular profile of the 15th harmonic from 2D PIC simulation.

wave mica waveplate. The waveplate was placed after the deformable mirror before the beam entered the vacuum chamber. A reference shot was taken by rotating the waveplate such that one of the axes was aligned with the horizontal polarization of the beam, leaving the polarization unaffected. The waveplate was then rotated 45° to produce vertical polarization (S-polarization on target). The data from both shots is shown in Fig. 6.11. The reference shot (upper figures) shows the same harmonic structure as shots taken with no waveplate (see Fig. 6.4). The UV emission of the S-polarized shot (lower figures) is approximately 30 times weaker and shows no harmonic structure.

As described in the introduction, in the oscillating mirror model, S-polarization is capable of generating odd-harmonic orders via the relativistic $\mathbf{v}\times\mathbf{B}$ force. In principle the $\mathbf{v}\times\mathbf{B}$ force should also be capable of driving electron bunches into the target and generating harmonics via coherent wake emission. However, at intensities where the $\mathbf{v}\times\mathbf{B}$ force is sufficient to generate significant harmonics, relativistic harmonics are expected to dominate those generated by CWE. The intensity scaling data presented above suggests that the intensity is below this level, so the lack of harmonics from S-polarized driving is not unexpected.

In the event that S-polarized driving produces differently polarized harmonics (which it does in the oscillating mirror model), the loss of signal cannot be attributed to the detection system. As discussed earlier, the efficiency of the grating is well approximated by scalar diffraction, and the near normal incidence eliminates any other polarization effects that might occur on the grating. The only other detection components, the aluminum filter and MCP, are used at normal incidence and therefore are polarization independent.

The behavior of circular polarization was also investigated, again using a mica waveplate. The waveplate was placed after the deformable mirror, before the beam entered the vacuum chamber. As before, a reference shot was taken (Fig. 6.12b) with

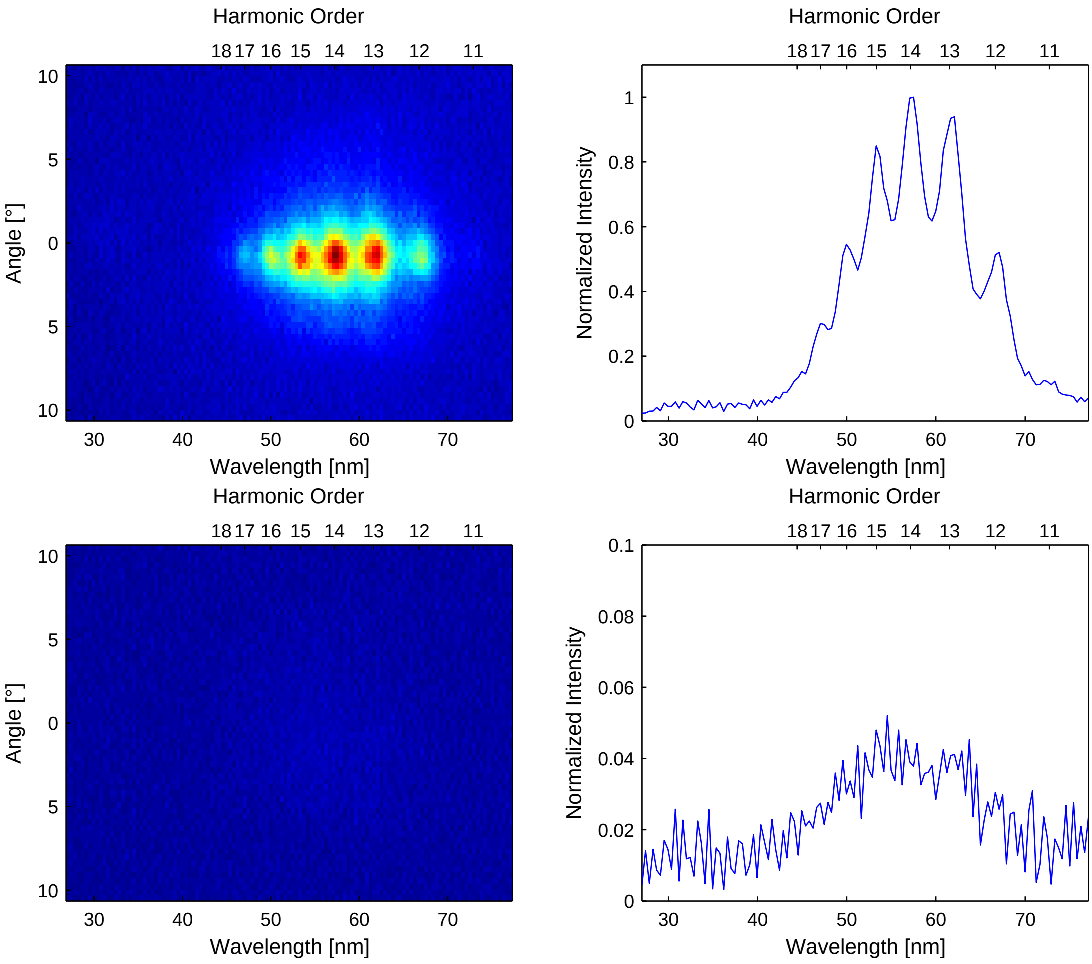

Figure 6.11: Comparison of P- and S-polarization driving. S-polarization (lower figures) produces weak UV emission with no resolvable harmonic structure compared to P-polarization (upper figures).

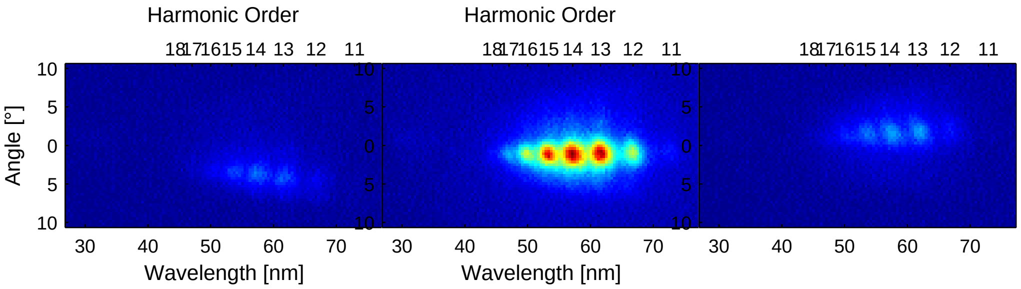

Figure 6.12: Harmonic spectra for left and right circular polarization (a and c, handedness unknown) compared to P-polarization (b).

one of the axes aligned with the horizontal beam polarization. The waveplate was then rotated 45° one direction (Fig. 6.12a) and 45° the other direction (Fig. 6.12c). The exact handedness of the circular polarizations was unknown.

The behavior of circular polarization is quite distinct from that of both linear polarizations. Rather than eliminating the harmonic signal, circular polarization changed the angular distribution of the spectrum. The central $\sim 5°$ of the emission was eliminated for either handedness. However, for one circular orientation the spectrum below 2.5° was retained, while for the other the spectrum above 2.5° was retained. The loss of the central spectrum greatly reduced the signal, but there was no change in the nature of the orders present. As mentioned above for S-polarization, the difference in signal cannot be attributed to polarization dependence of the detection system.

The reason for this behavior is unknown. The selection rules of the oscillating mirror model predict both S- and P-polarized harmonics of all orders for circularly polarized driving. The polarization of the harmonics generated here is unknown, but the spectra in Figs. 6.12a, and 6.12c clearly show all orders. The peculiar angular emission is likely due to the high-NA focusing. As discussed earlier, the polarization at focus, even for linear polarization prior to the paraboloid, is complex. When circular polarization is incident on the paraboloid, the asymmetry of reflections and the differing phase shift for S- and P-polarization from the metallic surface may lead to a very complicated polarization at focus.

6.5.5 Target position

The most significant experimental difficulty in working with high-NA optics is the extremely short depth of field. The Rayleigh range of a Gaussian beam is given by the formula

$$z_{\mathrm{R}} = \frac{\pi w_0^2}{\lambda} \tag{6.22}$$

For $f/1.4$ focusing the Gaussian beam formulation is still approximately correct. The Rayleigh range for the $f/1.4$ focus in these experiments is approximately 2 μm. This places a significant demand on the mechanics involved in finding and maintaining the proper position of the target, especially when operating at the speeds necessary for high repetition rates. The best method of finding the proper target position has proven to be optimization of some relevant signal (e.g. x-rays or 2nd harmonic) or direct optimization of the signal of interest, in this case harmonics. Fig. 6.13 shows several high-harmonic spectra taken at various positions of the target.

While the harmonics remain detectable as much as 10 μm from the optimum position, a shift of only 2 μm leads to a noticeable drop in intensity. In addition, as the target is moved, the shape and divergence of the harmonics gradually changes. The harmonics at positions 6 and 10 μm in the figure completely fill the acceptance angle of the grating.

In many laser experiments the intensity of an interaction can be changed by working at a different point along the beam focus. In these experiments, the intensity certainly drops as the target is moved off of focus. However, the near field profile of a high-NA beam does not behave smoothly off of focus. The drop in signal must be

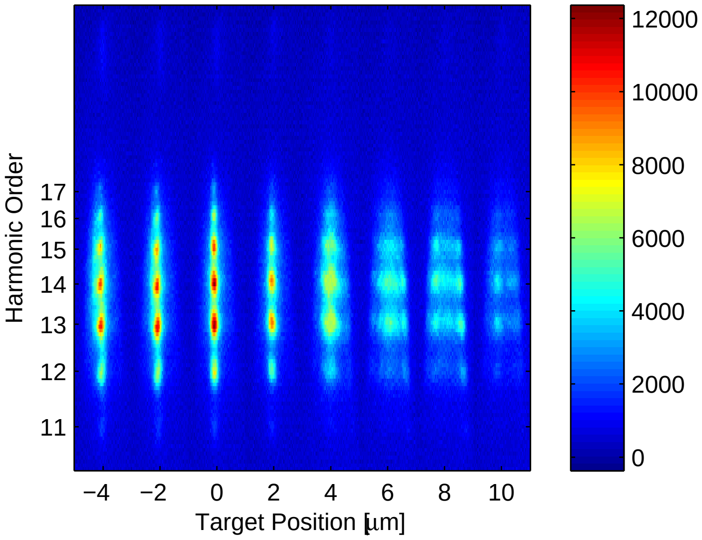

Figure 6.13: High-harmonic spectra taken as the target is moved through focus. The zero position was chosen post-acquisition to correspond to the best spectrum.

due in large part to the drop in intensity, but the distortion of the harmonic shape probably has more to do with the shape of the driving beam off of focus.

6.5.6 Harmonic generation from metallic targets

The use of glass targets is motivated primarily by their higher damage thresholds (several tens of J/cm^2 for ns pulses). Higher damage thresholds reduce the formation of a pre-plasma by the nanosecond ASE and picosecond pedestal prior to the arrival of the main pulse. However, the desire to perform experiments on targets of varying density leads to the consideration of metals and lower density dielectrics as targets.

Hydrocarbon targets have been used to demonstrate the effect of electron density on the harmonic order of coherent wake emission [37]. It has been proposed that lower density targets can provide better conditions for harmonic generation via the relativistic oscillating mirror effect [41]. Little attention however has been paid to metallic targets, owing to their high absorption (relative to dielectrics) and weakly bound electrons, leading to lower damage thresholds and higher pulse contrast re-

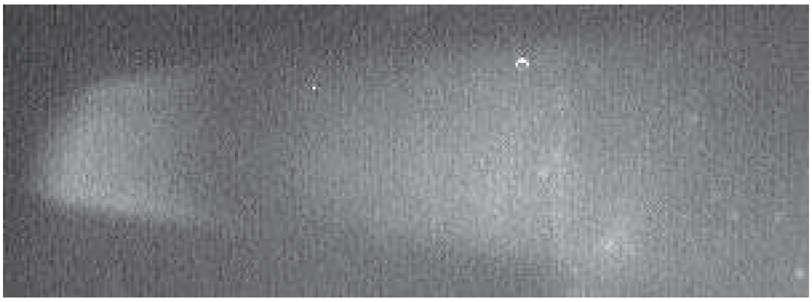

Figure 6.14: UV spectrum using a bulk aluminum target. The dark band is due to a null in diffraction efficiency at 72 nm.

quirements.

The success of harmonic generation in the work here from glass targets with no contrast enhancement mechanisms prompted further experiments employing aluminum targets. Aluminum was chosen for its ready availability, flatness, similar atomic number to silicon, and similar density to glass.

Two experiments using aluminum were conducted. In the first, a bulk, unprotected aluminum target was used. A typical spectrum is shown in Fig. 6.14. No harmonic lines are distinguishable (compare to Fig. 6.5). The single narrow feature is a strong atomic emission line at 106 nm.

The divergence of the emission from the bulk aluminum target cannot be compared to that of the harmonics shown in Fig. 6.4. The experimental run that produced Fig. 6.14 was performed before the sensitivity of the divergence to target position was understood. A second experiment was performed to correct this problem. By coating half of a fused silica wedge with approximately 1 μm of aluminum, the harmonics from glass and aluminum could be directly compared without adjusting the target position or even breaking vacuum.

An identical experimental arrangement was employed to that used for glass. Alignment and optimization were first performed on the uncoated half of the target. Harmonics in the aluminum filter transmission window (> 11th order) were generated (Fig. 6.15a). The target was then translated only a few hundred microns to expose

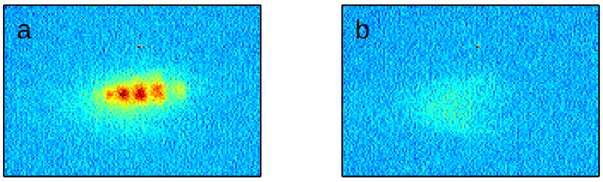

Figure 6.15: Harmonic spectra from glass (a) and aluminum (b).

the aluminum half (Fig. 6.15b).

The strength of the harmonics from the glass half of the target was not as great as it was from the bulk SiO_2 target. This may have been due to the poorer surface quality of the wedge compared to that of the bulk glass target used during the other runs. In any case, the 17th harmonic is still detectable and all of the harmonics still have a divergence of $\sim 3^\circ$. In contrast, the UV emission from the aluminum coated half of the target is much weaker and not in the form of harmonics. Nor is it emitted as a low-divergence beam. The simplest explanation is that the lower damage threshold of aluminum leads to a longer scale length, and perhaps a more turbulent plasma. The UV emission in Fig. 22b is simply continuum emission from a hot plasma. The difference between glass and aluminum results is consistent with earlier experiments comparing the 2nd harmonic and fast electrons emitted from glass and aluminum under similar conditions [62].

6.5.7 Scale-length

No tools were available at the time of this experiment to quantitatively determine the role of scale-length in high-harmonic generation. As a simple test, the final Pockels cell of the λ^3 system was defeated, allowing additional ASE and prepulses from prior roundtrips in the regenerative amplifier to arrive on target. The nearest prepulse occurs at 34 ns (the others occur at integer multiples of this interval, the round trip time of the amplifier) and contains approximately 10^{-4} times the energy of the main pulse when not attenuated by the Pockels cell. Despite this significant addition of ASE and prepulse energy, no change was observed in the generation of high-harmonics.

In previous experiments, the scale-length was shown to have a significant effect on the production of the 2nd and 3rd harmonic as well as the flux and spectrum of fast electron beams [62]. In those experiments, an intentional prepulse was introduced along a second beam line. The pulse was focused to a spot size of approximately 30 μm to generate a smooth plasma compared to the 1 μm focus of the main beam. The prepulse intensity was approximately 10^{14} W/cm^2 and its arrival prior to the main pulse was adjustable from 0 ps to $>$ 160 ps. Fig. 6.16 shows images of the 2nd harmonic for various prepulse delays.

One-dimensional HYADES simulations predicted a temperature of $\sim$20 eV and effective charge state of $Z^* \approx 3$. Assuming that the ionized plasma travels out from the target at the ion sound velocity:

$$\begin{aligned} c_s &= \sqrt{\frac{Z^* k T_e}{m_i}} \qquad (6.23) \\ &= 9.79 \times 10^5 \sqrt{\frac{Z^* T_e}{\mu}} \qquad (6.24) \end{aligned}$$

The plasma scale length can be estimated as

$$L = c_s \tau \qquad (6.25)$$

where τ is the prepulse delay. For the prepulse parameters listed above, the ion sound speed is 1.4×10^6 cm/s $= 1.4 \times 10^2$ μm/ps.

The optimum prepulse delay of 16 ps produces a second harmonic beam with a

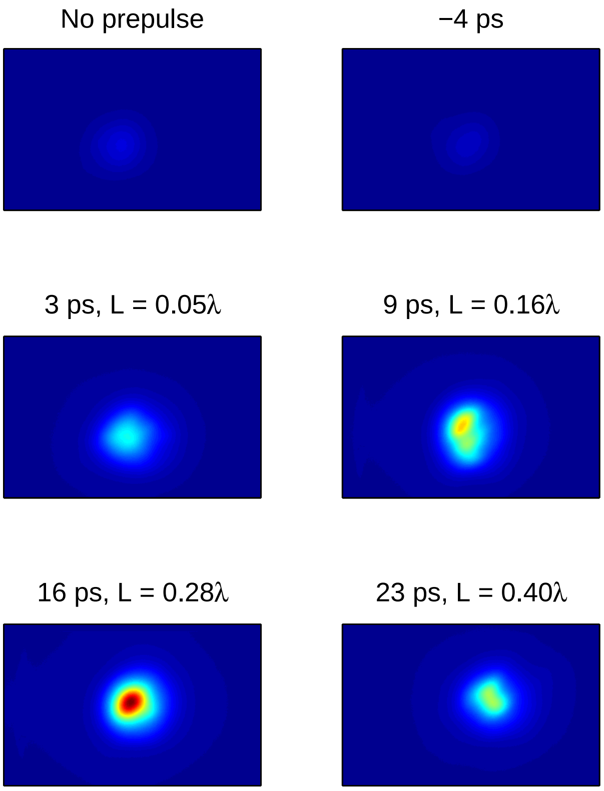

Figure 6.16: Second harmonic beam profile for six different prepulse delays and predicted scale lengths. All images are displayed on the same scale.

peak intensity approximately 10 times stronger than that for the case of no prepulse. The increase in 2nd and 3rd harmonic suggests that the intrinsic scale-length produced by the main beam contrast is shorter than optimum for the production of harmonics. This is encouraging, and suggests an approach for increasing the conversion efficiency of high-order harmonics.

6.5.8 Harmonic origin

The exact origin of the harmonics (CWE or relativistic) is unclear. The primary means of distinguishing between the two is by observation of a CWE harmonic cutoff at the maximum plasma frequency [37]. Fully ionized fused silica has an electron density of $n_e = 6.6 \times 10^{23}$ cm^{-3}. This corresponds to a plasma frequency of $\omega_{pe} = (4\pi e^2 n_e/m_e)^{(1/2)} = 4.6 \times 10^{16}$ rad/fs or $\lambda_{pe} = 2\pi c\omega_{pe} = 41$ nm, approximately the 20th harmonic of 800 nm. Unfortunately, this occurs very near a null in the efficiency of the diffraction grating (see Fig. 13), making it difficult to determine if the loss of harmonics at that wavelength is gradual or abrupt.

The scaling of conversion efficiency with intensity (Fig 6.6) suggests that the dominant mechanism is CWE. However, the scaling matched a higher power law exponent than that observed at lower intensities where CWE is expected to dominate. This is evidence that the dominant mechanism is beginning to transition from CWE to relativistic at the highest intensities employed in these experiments (10^{18} W/cm^2). Finally, the spectra acquired using different driving polarizations, especially S-polarization, suggest that relativistic mirror effects are not dominant. At truly relativistic intensities the $\mathbf{v} \times \mathbf{B}$ force should generate measurable odd-order harmonics.

6.5.9 Isolated attosecond pulse generation

The polarization dependence leads one to consider the possibility of generating isolated attosecond pulses using long (∼20–30 fs) driving pulses using polarization techniques demonstrated in gas harmonics. By combining two delayed, counter-rotating circular polarizations a long pulse with only a few—even a single—linearly polarized cycle can be created [63]. Because circular polarization does not generate gas harmonics, the few cycles of linear polarization are the only sources.

The same type of experiment may be possible with solid target harmonics and has been studied numerically [64]. While circular polarization did not eliminate the harmonic signal in the experiments presented here, it did change its angular emission. By collecting only the central 5° of the emission, the signal generated by one cycle of linear polarization (hopefully in the form of a sub-femtosecond pulse) could be separated from the signal generated by the other cycles of circular polarization.

It must be noted that in theory all driving polarizations generate harmonics by the relativistic moving mirror at sufficiently high intensity. Whether the behavior of circular polarization in these experiments is a result of the tight focusing and whether it continues to hold at higher intensities remains to be seen.

6.6 Conclusions and future work

In conclusion, harmonics of the 800 nm λ^3 system up to the 18th order have been observed from solid targets using millijoule pulses for the first time. An energy conversion efficiency of 2×10^{-7} per harmonic was measured. This is comparable to current efficiencies achieved in gas harmonic experiments, but has the advantage of being scalable to much higher intensities, where the conversion efficiency should also increase. Despite using a high-NA focus to achieve the necessary intensity, the harmonics were emitted with much lower divergences of approximately 3° (full angle), making the capture and manipulation of the harmonic beam considerably easier. The low energy of the λ^3 system and the lack of contrast enhancement mechanisms make this harmonic source very accessible and operable at high repetition rates. Similar systems operating at multi-kilohertz repetition rates should be capable of producing comparable harmonics with higher brightness.

Energy scaling data was presented and the effect of polarization was described. Modification of the angular emission for circular polarization suggests that a polarization gating technique like that used in gas harmonics may also be used on solid targets to generate single sub-femtosecond pulses using long (> 20 fs) driving pulses. Further investigation, possibly in conjunction with 3D PIC simulations, may yield an explanation for the unique angular character of the emission generated by circularly polarized driving pulses.

Multiple approaches are available for attempting to increase the conversion efficiency. Related experiments on lower order harmonics and fast electrons provide evidence that the intrinsic scale length in these experiments was shorter than optimal. By introducing an intentional prepulse to control the scale length, better conditions for harmonic generation may be found. In addition, relatively straightforward improvements to the laser system should be capable of decreasing the focus size and pulse duration, leading to a higher intensity and higher conversion efficiency.

Additional work remains to be done in investigating the role of target material in the high-harmonic generation process. Experiments on aluminum have shown a significant decrease in the strength and spatial quality of harmonics compared to those from glass. Whether this is due simply to the lower damage threshold of metals or to important differences in the ionization process is not yet certain. A wealth of other data stands to be collected now that such easy access to solid target harmonics is available. This includes polarization and temporal characterization of the harmonics, experiments on lower density targets, correlation to fast electrons, and experiments and simulations involving different numerical aperture focusing geometries.

CHAPTER VII

Conclusion

The use of high-NA focusing optics and adaptive optics has opened up the regime of relativistic laser-plasma interactions to a much broader class of systems. The work described here has helped to advance this technology through a consistent set of experiments. First, a high contrast amplifier was designed and built to reduce the problem of amplified spontaneous emission. Second, a method of extending filamentation compression to higher energies through the use of differential pumping was investigated. This method may allow the generation of few-cycle TW pulses, increasing the achievable intensity with high-repetition rate systems. Third, an adaptation of the MIIPS ultrashort pulse measurement technique was proposed and demonstrated. By using the compressor gratings already found in most CPA systems the complexity and cost of implementing ultrashort pulse measurements were reduced. Fourth, a new technique of optimizing the configuration of a deformable mirror for high-intensity focusing was implemented. By operating at full power and employing no additional optics, this technique provides a simpler, more accurate method of correcting wavefront aberrations to achieve the highest possible intensities. Finally, the previously mentioned work led to the first demonstration of high repetition rate, high-harmonic generation from solid targets. Harmonics up to the 18th order were generated with conversion efficiencies similar to gas harmonics.

Several approaches to increasing the harmonic yield are available and should lead to construction of a high brightness source of coherent EUV/XUV harmonics and sub-femtosecond pulses.

First among these is improving the temporal duration of the driving pulse. The grating based MIIPS technique revealed significant errors in the spectral phase of the λ^3 system. As much correction as possible was made using the degrees of freedom available in the compressor (separation and rotation), however, higher-order corrections are necessary to achieve a transform-limited pulse duration. The system now employs an acousto-optic programmable dispersive device (Fastlite Dazzler). In the near future the remaining spectral phase errors should be corrected, producing sub-30 fs compressed pulses. This should increase the focused intensity by approximately a factor of two, leading to improved harmonic conversion efficiency.

Secondly, a smaller focus should be achievable by modification of the post-compression telescope and the use of a faster paraboloid. The system currently uses an underfilled $f/1.4$ paraboloid. By further expanding the beam the focal size can be reduced, increasing the intensity. Also, a faster paraboloid will in principle produce a smaller focus. Off-axis paraboloids at least as fast as $f/0.8$ are available. These paraboloids have been tested on the system in the past with limited success. However, the new, simpler method of focus optimization may help in implementing higher-NA optics.

Finally, state-of-the-art amplifiers are capable of delivering much higher pulse energies at kilohertz repetition rates. The λ^3 system is currently being upgraded to produce as much as 15 mJ per pulse at 500 Hz. All else being equal, the focused intensity should exceed 10^{19} W/cm^2, a significant increase beyond what was used in the experiments discussed here. With these developments it is expected that high repetition rate solid target harmonics will soon supplant gas harmonic sources for many applications.

APPENDICES

APPENDIX A

Wavelet Analysis of SPIDER Traces

The following is work that was presented at the 2009 Conference on Lasers and Electro-optics (CLEO). It has not been given a full chapter for two reasons: it is not closely tied to the rest of the work and its impact on the field is less significant.

Fringe analysis is an important tool in many optical techniques including linear spectral dispersion measurements, spectral interferometry for direct electric field reconstruction (SPIDER) [65], and other techniques involving spectral interferometry. In general, fringe analysis involves extracting high frequency fringe data from a low frequency spectral envelope, where the fringe frequency must be sufficiently high to prevent overlap between the high and low frequencies. However, spectral interferograms are often interpolated from a semi-evenly-spaced wavelength domain (e.g. from a spectrometer) to an evenly-spaced frequency domain before analysis to match functional forms best represented in an evenly-spaced frequency domain and to allow the use of fast Fourier transforms. When the fringe density is near the Nyquist sampling criteria this interpolation introduces significant errors.

One method of analyzing the fringe data of a SPIDER trace is by wavelet analysis [66]. A set of pulses with varying carrier frequencies is compared against the fringes. The instantaneous frequency at each point in the interferogram is taken to be the

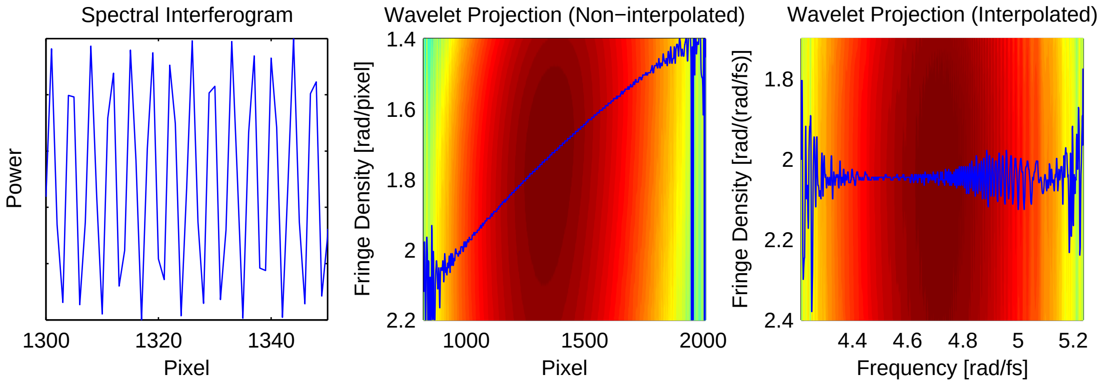

Figure A.1: Left: subset of a high fringe density spectral interferogram in the evenly-spaced wavelength domain of a spectrometer. Middle: fringe density from non-interpolated interferogram. Right: fringe density from interferogram interpolated to an evenly-spaced frequency domain via cubic spline interpolation.

carrier frequency of that wavelet which best matched the fringes at that point.

Fig. A.1 shows the difference between extracting fringe density in the native domain of the interferogram and in an evenly-spaced frequency domain. The interferogram (left) contains high density fringes, pushing the limits of the Nyquist sampling critera as evidenced by the loss of fringe contrast. Wavelet based analysis of the interferogram in its native pixel domain (middle) yields an accurate fringe density. However, if the interferogram is interpolated to an evenly-spaced frequency domain a significant amount of noise occurs in the fringe density analysis (right).

This noise is due to the fact that the interpolation cannot accurately reproduce the high density fringes. The errors can be reduced by interpolating to a denser set of points, however the necessary increase in density (typically greater than 4 times) leads to slower algorithm performance. In addition, even if the interpolation density is very high, direct analysis of the fringes is less susceptible to reduced fringe contrast than interpolation.

The phase of the fringes can be extracted from the fringe density via integration or by unwrapping of the wavelet phase. Wavelet based analysis was chosen here because the interpolation errors are easier to show on a wavelet projection map. Fourier transform fringe analysis could also be performed in the non-interpolated domain. In either case, the resulting fringe density or phase is a much smoother function than the interferogram and can be interpolated to the desired domain with much higher accuracy.

In the case of SPIDER, the uninterpolated fringe phase can be integrated to obtain the spectral phase by recognizing that the differential element in the integral depends on the domain in which the fringe phase is represented. In the frequency domain this integral takes the form

$$\phi(\omega) = \int_{\omega_0}^{\omega} [\theta(\Omega) - \Omega\tau] d\Omega \tag{A.1}$$

where ϕ is the spectral phase, θ is the interferogram fringe phase, and τ is the delay in the double pulse arm of the SPIDER. If the fringe phase is evaluated in evenly-spaced wavelength for example, the integral would be

$$\phi(\omega) = \int_{2\pi c/\omega_0}^{2\pi c/\omega} \left[\theta\left(\frac{2\pi c}{\lambda}\right) - \frac{2\pi c}{\lambda}\right] \frac{d\Omega}{d\lambda} d\lambda \tag{A.2}$$

where $d\Omega/d\lambda = -2\pi c/\lambda^2$. The interpolation can then be performed on the spectral phase, an even smoother function. In fact, the integration can be performed in an arbitrary domain, x, by replacing $d\Omega$ with $(d\Omega/dx)dx$.

Interpolation of high density fringes in a spectral interferogram leads to errors which can be avoided by performing fringe analysis in the original domain of the data. The interpolation can then be performed later in the analysis on smoother data. In the case of SPIDER, a slight integral modification allows the calculation of the spectral phase with no interpolation at all. Applications requiring high accuracy fringe retrieval will benefit from the lack of errors introduced by interpolation.

APPENDIX B

Grating-based MIIPS Algorithm

The following MATLAB code implements the grating-based MIIPS algorithm. The algorithm accepts a set of spectra and vectors specifying the grating separation and incidence angle for each spectra. The inherent group delay dispersion (GDD), $\phi''(\omega)$, is calculated as described in Chapter III:

$$\phi''(\omega) = -\theta''(\omega) \tag{B.1}$$

where $\theta''(\omega)$ is the applied GDD that produced the strongest signal at 2ω given by [12]

$$\theta'' = -G\frac{N^2\lambda^3}{\pi c^2 \cos^3\beta} \tag{B.2}$$

$$\sin\gamma - \sin\beta = m\lambda N \tag{B.3}$$

Numerical integration of the GDD to obtain the group delay and of the group delay to obtain the phase is performed as

$$\phi'[n] = \begin{cases} \phi'', & n = 0 \\ \phi'[n-1]\phi''[n]\frac{d\omega[n]}{dn}, & n \neq 0 \end{cases} \tag{B.4}$$

$$\phi[n] = \begin{cases} \phi', & n = 0 \\ \phi[n-1] + \phi'[n]\frac{d\omega[n]}{dn}, & n \neq 0 \end{cases} \tag{B.5}$$

The factor $d\omega[n]/dn$ in Eqs. (B.4) and (B.5) accounts for the uneven frequency spacing of the spectral data. The code here assumes that the wavelengths of the spectral data can be described by a polynomial:

$$\lambda[n] = \sum_{m=0}^{M} a_m n^m \tag{B.6}$$

where a_m is the set of polynomial coefficients. The wavelengths of most spectrometers can be described by Eq. (B.6). The frequency step can then be calculated:

$$\begin{aligned} \frac{d\omega[n]}{dn} &= \frac{d\omega}{d\lambda}\frac{d\lambda[n]}{dn} && \text{(B.7)} \\ &= -\frac{2\pi c}{\lambda[n]}\sum_{m=0}^{M} a_m m n^{m-1} && \text{(B.8)} \end{aligned}$$

```
% Inputs
% D.files  : names of the files
% D.G      : grating separations [um]
% D.gamma  : incidence angles [deg]
% D.G0     : grating separation [um] at which to evaluate the phase
% D.gamma0 : incidence angle [deg] at which to evaluate the phase
```

```
% D.a      : wavelength coefficients

% Outputs
% D.M      : spectra array
% D.lambda : wavelengths [um]
% D.phipp  : group delay dispersion [fs]
% D.phip   : group delay [fs]
% D.Y      : ridge
% D.p      : index of maximum ridge pixel

function D = MIIPS(D)

for m = 0:(numel(D.files) - 1)
[A, F, H] = importdata(D.files(m));
D.M(m + 1, :) = A.data(:, 2);
end

[D.Y, I] = max(D.M);

% The factor of two in front of the following wavelength
% coefficients is to move the calculation back up to the
% fundamental.
a = 2 * D.a;
lambda = polyval(a, 0:(size(D.M, 2) - 1)) / 1000;
dwdn = -2 * pi * 0.3 ./ lambda .^ 2 .* ...
polyval(((length(a) - 1):-1:1) .* a(1:(end - 1)), ...
0:(size(D.M, 2) - 1)) / 1000;
```

```
% diffracted angle [deg]
theta = asind(sind(D.gamma) - lambda * D.N);
theta0 = asind(sind(D.gamma0) - lambda * D.N);

D.phipp = D.G(I) * D.N ^ 2 .* lambda .^ 3 ./ ...
(pi * 0.3 ^ 2 * cosd(theta(I)) .^ 3) - ...
D.G0 * D.N ^ 2 .* lambda .^ 3 ./ ...
(pi * 0.3 ^ 2 * cosd(theta0) .^ 3); % GDD [fs]

% Integrate to obtain the group delay.
D.phip = cumsum(D.phipp .* dwdn); % group delay [fs]

% Integrate to obtain the phase.
D.phi = cumsum(D.phip .* dwdn); % phase [rad]

D.lambda = lambda;

end
```

BIBLIOGRAPHY

BIBLIOGRAPHY

[1] K.-H. Hong, B. Hou, J. A. Nees, E. Power, and G. A. Mourou. Generation and measurement of $> 10^8$ intensity contrast ratio in a relativistic kHz chirped-pulse amplified laser. *Appl. Phys. B*, 81(4):447–457, 2005.

[2] J. Itatani, J. Faure, M. Nantel, G. Mourou, and S. Watanabe. Suppression of the amplified spontaneous emission in chirped-pulse-amplification lasers by clean high-energy seed-pulse injection. *Optics Communications*, 148(1-3):70 – 74, 1998.

[3] Aurélie Jullien, Olivier Albert, Frédéric Burgy, Guy Hamoniaux, Jean-Philippe Rousseau, Jean-Paul Chambaret, Frédérika Augé-Rochereau, Gilles Chériaux, Jean Etchepare, Nikolay Minkovski, and Solomon M. Saltiel. 10^{-10} temporal contrast for femtosecond ultraintense lasers by cross-polarized wave generation. *Opt. Lett.*, 30(8):920–922, 2005.

[4] D. F. Price, R. M. More, R. S. Walling, G. Guethlein, R. L. Shepherd, R. E. Stewart, and W. E. White. Absorption of ultrashort laser pulses by solid targets heated rapidly to temperatures 1–1000 ev. *Phys. Rev. Lett.*, 75(2):252–255, Jul 1995.

[5] G. Doumy, F. Quéré, O. Gobert, M. Perdrix, Ph. Martin, P. Audebert, J. C. Gauthier, J.-P. Geindre, and T. Wittmann. Complete characterization of a plasma mirror for the production of high-contrast ultraintense laser pulses. *Phys. Rev. E*, 69(2):026402, 2004.

[6] V. Yanovsky, C. Felix, and G. Mourou. Why ring regenerative amplification (regen)? *Applied Physics B: Lasers and Optics*, 74(0):s181–s183, 2002.

[7] N. V. Didenko, A. V. Konyashchenko, A. P. Lutsenko, and S. Y. Tenyakov. Contrast degradation in a chirped-pulse amplifier due to generation of prepulses by postpulses. *Opt. Express*, 16(5):3178–3190, 2008.

[8] D. Du, X. Liu, G. Korn, J. Squier, and G. Mourou. Laser-induced breakdown by impact ionization in sio[sub 2] with pulse widths from 7 ns to 150 fs. *Applied Physics Letters*, 64(23):3071–3073, 1994.

[9] C. Iaconis and I.A. Walmsley. Spectral phase interferometry for direct electric-field reconstruction of ultrashort optical pulses. *Opt. Lett.*, 23(10):792–794, 1998.

[10] D.J. Kane and R. Trebino. Characterization of arbitrary femtosecond pulses using frequency-resolved optical gating. *Quantum Electronics, IEEE Journal of*, 29(2):571 –579, feb 1993.

[11] Yves Coello, Vadim V. Lozovoy, Tissa C. Gunaratne, Bingwei Xu, Ian Borukhovich, Chien hung Tseng, Thomas Weinacht, and Marcos Dantus. Interference without an interferometer: a different approach to measuring, compressing, and shaping ultrashort laser pulses. *J. Opt. Soc. Am. B*, 25(6):A140–A150, 2008.

[12] E. Treacy. Optical pulse compression with diffraction gratings. *Quantum Electronics, IEEE Journal of*, 5(9):454–458, sep 1969.

[13] A. Baltuska, M.S. Pshenichnikov, and D.A. Wiersma. Second-harmonic generation frequency-resolved optical gating in the single-cycle regime. *Quantum Electronics, IEEE Journal of*, 35(4):459 –478, apr 1999.

[14] Bingwei Xu, Jess M. Gunn, Johanna M. Dela Cruz, Vadim V. Lozovoy, and Marcos Dantus. Quantitative investigation of the multiphoton intrapulse interference phase scan method for simultaneous phase measurement and compensation of femtosecond laser pulses. *J. Opt. Soc. Am. B*, 23(4):750–759, 2006.

[15] Anthony E. Siegman. *Lasers*. University Science Books, 55D Gate Five Road, Sausalito, CA 94965, 1986.

[16] Sterling Backus, Charles G. Durfee III, Gerard Mourou, Henry C. Kapteyn, and Margaret M. Murnane. 0.2-tw laser system at 1khz. *Opt. Lett.*, 22(16):1256–1258, 1997.

[17] C. P. J. Barty, G. Korn, F. Raksi, C. Rose-Petruck, J. Squier, A.-C. Tien, K. R. Wilson, V. V. Yakovlev, and K. Yamakawa. Regenerative pulse shaping and amplification of ultrabroadband optical pulses. *Opt. Lett.*, 21(3):219–221, 1996.

[18] R. Butkus, R. Danielius, A. Dubietis, A. Piskarskas, and A. Stabinis. Progress in chirped pulse optical parametric amplifiers. *Appl. Phys. B*, 79(6):693–700, Oct 2004.

[19] Claude Rolland and P. B. Corkum. Compression of high-power optical pulses. *J. Opt. Soc. Am. B*, 5(3):641–647, 1988.

[20] M. Nisoli, S. De Silvestri, O. Svelto, R. Szipöcs, K. Ferencz, Ch. Spielmann, S. Sartania, and F. Krausz. Compression of high-energy laser pulses below 5 fs. *Opt. Lett.*, 22(8):522–524, 1997.

[21] C.P. Hauri, W. Kornelis, F.W. Helbing, A. Heinrich, A. Couairon, A. Mysyrowicz, J. Biegert, and U. Keller. Generation of intense, carrier-envelope phase-locked few-cycle laser pulses through filamentation. *Appl. Phys. B*, 79(6):673–677, Oct 2004.

[22] A. Couairon, J. Biegert, C. P. Hauri, W. Kornelis, F. W. Helbing, U. Keller, and A. Mysyrowicz. Self-compression of ultra-short laser pulses down to one optical cycle by filamentation. *J. Mod. Opt.*, 53(1):75–85, 2006.

[23] P. Béjot, J. Kasparian, S. Henin, V. Loriot, T. Vieillard, E. Hertz, O. Faucher, B. Lavorel, and J.-P. Wolf. Higher-order kerr terms allow ionization-free filamentation in gases. *Phys. Rev. Lett.*, 104(10):103903, Mar 2010.

[24] Gadi Fibich, Shmuel Eisenmann, Boaz Ilan, and Arie Zigler. Control of multiple filamentation in air. *Opt. Lett.*, 29(15):1772–1774, 2004.

[25] J M Beckers. Adaptive optics for astronomy: Principles, performance, and applications. *Annual Review of Astronomy and Astrophysics*, 31(1):13–62, 1993.

[26] S.-W. Bahk, P. Rousseau, T. A. Planchon, V. Chvykov, G. Kalintchenko, A. Maksimchuk, G. A. Mourou, and V. Yanovsky. Generation and characterization of the highest laser intensities (10^{22} w/cm^2). *Opt. Lett.*, 29(24):2837–2839, 2004.

[27] O. Albert, H. Wang, D. Liu, Z. Chang, and G. Mourou. Generation of relativistic intensity pulses at a kilohertz repetition rate. *Opt. Lett.*, 25(15):1125–1127, 2000.

[28] T. A. Planchon, W. Amir, J. J. Field, C. G. Durfee, J. A. Squier, P. Rousseau, O. Albert, and G. Mourou. Adaptive correction of a tightly focused, high-intensity laser beam by use of a third-harmonic signal generated at an interface. *Opt. Lett.*, 31(14):2214–2216, 2006.

[29] D. S. Bethune. Optical second-harmonic generation in atomic vapors with focused beams. *Phys. Rev. A*, 23(6):3139–3151, Jun 1981.

[30] Martynas Beresna, Peter G. Kazansky, Yuri Svirko, Martynas Barkauskas, and Romas Danielius. High average power second harmonic generation in air. *Applied Physics Letters*, 95(12):121502, 2009.

[31] J. Bernhardt, P.T. Simard, W. Liu, H.L. Xu, F. Thberge, A. Azarm, J.F. Daigle, and S.L. Chin. Critical power for self-focussing of a femtosecond laser pulse in helium. *Optics Communications*, 281(8):2248 – 2251, 2008.

[32] B. Walker, B. Sheehy, L. F. DiMauro, P. Agostini, K. J. Schafer, and K. C. Kulander. Precision measurement of strong field double ionization of helium. *Phys. Rev. Lett.*, 73(9):1227–1230, Aug 1994.

[33] S. Kohlweyer, G. D. Tsakiris, C. G. Wahlström, C. Tillman, and I. Mercer. Harmonic generation from solid-vacuum interface irradiated at high laser intensities. *Optics Communications*, 117(5-6):431 – 438, 1995.

[34] F. Quéré, C. Thaury, P. Monot, S. Dobosz, Ph. Martin, J.-P. Geindre, and P. Audebert. Coherent wake emission of high-order harmonics from overdense plasmas. *Phys. Rev. Lett.*, 96(12):125004, Mar 2006.

[35] D. von der Linde and K. Rzzewski. High-order optical harmonic generation from solid surfaces. *Appl. Phys. B*, 63(5):499–506, 1996.

[36] Alexander Pukhov. Strong field interaction of laser radiation. *Reports on Progress in Physics*, 66(1):47, 2003.

[37] Alexander Tarasevitch, Konstantin Lobov, Clemens Wünsche, and Dietrich von der Linde. Transition to the relativistic regime in high order harmonic generation. *Phys. Rev. Lett.*, 98(10):103902, Mar 2007.

[38] R. Lichters, J. Meyer ter Vehn, and A. Pukhov. Short-pulse laser harmonics from oscillating plasma surfaces driven at relativistic intensity. *Physics of Plasmas*, 3 (9):3425–3437, 1996.

[39] R. Fedosejevs, M. D. J. Burgess, G. D. Enright, and M. C. Richardson. Supercritical Density Profiles of CO_2-Laser-Irradiated Microballoons. *Phys. Rev. Lett.*, 43(22):1664–1667, Nov 1979.

[40] A. Tarasevitch, A. Orisch, D. von der Linde, Ph. Balcou, G. Rey, J.-P. Chambaret, U. Teubner, D. Klöpfel, and W. Theobald. Generation of high-order spatially coherent harmonics from solid targets by femtosecond laser pulses. *Phys. Rev. A*, 62(2):023816, Jul 2000.

[41] Natalia M. Naumova, John A. Nees, and Gerard A. Mourou. Relativistic attosecond physics. *Physics of Plasmas*, 12(5):056707, 2005.

[42] Roman V Volkov, Vyacheslav M Gordienko, Sergey A Magnitskiy, P G Oganyan, P A Oleinikov, Viktor T Platonenko, and A P Tarasevitch. Evolution of a high-temperature femtosecond surface plasma, recorded with time resolution. *Quantum Electronics*, 25(9):877, 1995.

[43] J.-C. Gauthier, J. P. Geindre, P. Audebert, S. Bastiani, C. Quoix, G. Grillon, A. Mysyrowicz, A. Antonetti, and R. C. Mancini. Theoretical and experimental studies of laser-produced plasmas driven by high-intensity femtosecond laser pulses. *The 38th annual meeting of the Division of Plasma Physics (DPP) of the American Physical Society*, 4(5):1811–1817, 1997.

[44] Jon T. Larsen and Stephen M. Lane. Hyades–a plasma hydrodynamics code for dense plasma studies. *Journal of Quantitative Spectroscopy and Radiative Transfer*, 51(1-2):179 – 186, 1994.

[45] Alexei Zhidkov, Akira Sasaki, Takayuki Utsumi, Ichirou Fukumoto, Toshiki Tajima, Fumikazu Saito, Yoichiro Hironaka, Kazutaka G. Nakamura, Ken-ichi Kondo, and Masatake Yoshida. Prepulse effects on the interaction of intense femtosecond laser pulses with high-Z solids. *Phys. Rev. E*, 62(5):7232–7240, Nov 2000.

[46] Charles Varin, Michel Piché, and Miguel A. Porras. Analytical calculation of the longitudinal electric field resulting from the tight focusing of an ultrafast transverse-magnetic laser beam. *J. Opt. Soc. Am. A*, 23(8):2027–2038, 2006.

[47] Melvin Lax, William H. Louisell, and William B. McKnight. From Maxwell to paraxial wave optics. *Phys. Rev. A*, 11(4):1365–1370, Apr 1975.

[48] L. W. Davis. Theory of electromagnetic beams. *Phys. Rev. A*, 19(3):1177–1179, Mar 1979.

[49] Scott M. Sepke and Donald P. Umstadter. Analytical solutions for the electromagnetic fields of tightly focused laser beams of arbitrary pulse length. *Opt. Lett.*, 31(17):2589–2591, 2006.

[50] R. Hörlein, S. G. Rykovanov, B. Dromey, Y. Nomura, D. Adams, M. Geissler, M. Zepf, F. Krausz, and G. D. Tsakiris. Controlling the divergence of high harmonics from solid targets: a route toward coherent harmonic focusing. *The European Physical Journal D*, 55(2):475–481, 2009.

[51] B. Dromey, D. Adams, R. Horlein, Y. Nomura, S. G. Rykovanov, D. C. Carroll, P. S. Foster, S. Kar, K. Markey, P. McKenna, D. Neely, M. Geissler, G. D. Tsakiris, and M. Zepf. Diffraction-limited performance and focusing of high harmonics from relativistic plasmas. *Nat. Phys.*, 5(2):146–152, 2009.

[52] N. M. Naumova, J. A. Nees, I. V. Sokolov, B. Hou, and G. A. Mourou. Relativistic generation of isolated attosecond pulses in a $\lambda 3$ focal volume. *Phys. Rev. Lett.*, 92(6):063902, Feb 2004.

[53] Edward H. Eberhardt. Gain model for microchannel plates. *Appl. Opt.*, 18(9):1418–1423, 1979.

[54] E. G. Loewen, M. Nevière, and D. Maystre. Grating efficiency theory as it applies to blazed and holographic gratings. *Appl. Opt.*, 16(10):2711–2721, 1977.

[55] Joseph W. Goodman. *Introduction to Fourier Optics*. The McGraw-Hill Companies, 1996.

[56] P. A. Norreys, M. Zepf, S. Moustaizis, A. P. Fews, J. Zhang, P. Lee, M. Bakarezos, C. N. Danson, A. Dyson, P. Gibbon, P. Loukakos, D. Neely, F. N. Walsh, J. S. Wark, and A. E. Dangor. Efficient extreme uv harmonics generated from picosecond laser pulse interactions with solid targets. *Phys. Rev. Lett.*, 76(11):1832–1835, Mar 1996.

[57] Paul Gibbon. Harmonic generation by femtosecond laser-solid interaction: A coherent “water-window” light source? *Phys. Rev. Lett.*, 76(1):50–53, Jan 1996.

[58] R. A. Fonseca, L. O. Silva, F. S. Tsung, V. K. Decyk, W. Lu, C. Ren, W. B. Mori, S. Deng, S. Lee, T. Katsouleas, and J. C. Adam. *OSIRIS: A Three-Dimensional, Fully Relativistic Particle in Cell Code for Modeling Plasma Based Accelerators*. Springer Berlin / Heidelberg, 2002. 342–351 pp.

[59] Ximao Feng, Steve Gilbertson, Hiroki Mashiko, He Wang, Sabih D. Khan, Michael Chini, Yi Wu, Kun Zhao, and Zenghu Chang. Generation of isolated attosecond pulses with 20 to 28 femtosecond lasers. *Phys. Rev. Lett.*, 103(18): 183901, Oct 2009.

[60] Yu Oishi, Masanori Kaku, Akira Suda, Fumihiko Kannari, and Katsumi Midorikawa. Generation of extreme ultraviolet continuum radiation driven by a sub-10-fs two-color field. *Opt. Express*, 14(16):7230–7237, 2006.

[61] B. Dromey, M. Zepf, A. Gopal, K. Lancaster, M. S. Wei, K. Krushelnick, M. Tatarakis, N. Vakakis, S. Moustaizis, R. Kodama, M. Tampo, C. Stoeckl, R. Clarke, H. Habara, D. Neely, S. Karsch, and P. Norreys. High harmonic generation in the relativistic limit. *Nat. Phys.*, 2(7):456–459, 2006.

[62] Aghapi G. Mordovanakis, James Easter, Natalia Naumova, Konstantin Popov, Paul-Edouard Masson-Laborde, Bixue Hou, Igor Sokolov, Gérard Mourou, Igor V. Glazyrin, Wojciech Rozmus, Valery Bychenkov, John Nees, and Karl Krushelnick. Quasimonoenergetic Electron Beams with Relativistic Energies and Ultrashort Duration from Laser-Solid Interactions at 0.5 kHz. *Phys. Rev. Lett.*, 103(23):235001, Dec 2009.

[63] M. Kovacev, Y. Mairesse, E. Priori, H. Merdji, O. Tcherbakoff, P. Monchicourt, P. Breger, E. Mvel, E. Constant, P. Salires, B. Carr, and P. Agostini. Temporal confinement of the harmonic emission through polarization gating. *The European Physical Journal D*, 26(1):79–82, 2003.

[64] S G Rykovanov, M Geissler, J Meyer ter Vehn, and G D Tsakiris. Intense single attosecond pulses from surface harmonics using the polarization gating technique. *New Journal of Physics*, 10(2):025025, 2008.

[65] C. Iaconis and I.A. Walmsley. Self-referencing spectral interferometry for measuring ultrashort optical pulses. *Quantum Electronics, IEEE Journal of*, 35(4): 501 –509, apr 1999.

[66] J. Bethge, C. Grebing, and G. Steinmeyer. A fast Gabor wavelet transform for high-precision phase retrieval in spectral interferometry. *Opt. Express*, 15(22): 14313–14321, 2007.